TORSIONAL OSCILLATOR FOR THE STUDY OF HELIUM THREE IN CONFINED GEOMETRIES

A Dissertation

Presented to the Faculty of the Graduate School

of Cornell University

in Partial Fulfillment of the Requirements for the Degree of

Doctor of Philosophy

by

Svetoslav Genchev Dimov

August 2009

TORSIONAL OSCILLATOR FOR THE STUDY OF HELIUM THREE IN CONFINED GEOMETRIES

Svetoslav Genchev Dimov, Ph.D.

Cornell University 2009

We have constructed a torsional oscillator for the study of the ^3He liquid in confined geometries by lithographically patterning a silicon wafer and anodically bonding it to a glass wafers. The liquid helium has been constrained to an annular cavity with diameter $1cm$ and height $640nm$.

The inertia of the normal fluid has been observed to be partially coupled to the oscillator at $160mK$ and to completely decouple below $100mK$. The decoupling is attributed to the specular scattering of the quasiparticles from the smooth surfaces of the cell.

An analysis of the surface topographies has been performed and comparison to a related experiment by Casey et. al. has been done.

BIOGRAPHICAL SKETCH

Svetoslav showed interest in the sciences from an early age. His interests led him to enroll in the ”National High School for Natural Sciences” in Sofia, Bulgaria. There he had the privilege to study under the supervision of nationally renowned scientists and university professors. After graduating high school he enrolled in the Sofia University as an Engineering Physics major and later transferred to SUNY - Stony Brook where he completed his undergraduate study in the field of high energy physics.

Svetoslav continued his education at Cornell University where he joined the low temperature group under the supervision of Professor Jeevak Parpia. Despite the number of glitches and countless worrisome hours spent in the basement of Clark Hall he has appreciated all the time and lessons learned. Svetoslav was fortunate to be one of the first students to work in the newly renovated Cornell NanoScale Science & Technology Facility. There he got addicted to the bunny suits and is determined to continue using those for years to come.

Svetoslav has accepted a position as a research engineer at Intel. Perhaps there he will be able to spend a little bit more time with his family.

To Stela for sharing the burden with me.

To Nicholai for making the burden meaningful.

To the rest of my family for being there.

ACKNOWLEDGEMENTS

I hardly expected what laid ahead of me when I started my graduate studies. Many hardships were overcome only with the help of others that I would like to acknowledge.

First and foremost I have to thank my advisor, Professor Jeevak Parpia. Jeevak has been patient with me beyond bounds one would expect. I have learned many things under his supervision.

I thank Professors Séamus Davis and Erich Mueller for serving on my Special Committee.

Eric Smith has been incredibly helpful for helping me get around many technical problems.

Discussions with Andrew Fefferman and Scott Verbridge have been instrumental for parts of this experiment.

TABLE OF CONTENTS

LIST OF TABLES

LIST OF FIGURES

CHAPTER 1

INTRODUCTION

1.1 Normal ^3He

The conventional hydrodynamic conditions require that the relative velocity of a fluid past a boundary goes to zero at the surface. However, for geometries where the volume to surface ratio is approximately equal to the mean free path, a correction is needed. The first order correction is described by the slip theory[2] which allows for a finite velocity mismatch between the boundary and the fluid. The slip amount is dependent on the nature of the fluid and the types of surface scattering. The smallest slip occurs when the scattering is diffuse. As the surfaces get smoother (increasing specular scattering) less momentum is transferred to the scattered particles and the slip increases.

As the ^3He fluid can have a long mean free path, the slip can substantially modify macroscopic quantities such as dissipation or frequency shift of a filled torsional oscillator. Therefore the understanding of the behavior of the ^3He flow near the boundary is very important.

Early measurements [3, 4] of the ^3He flow past a boundary have suggested that the scattering was diffuse for a wide range of materials and the slip was small. However the surfaces used there were machined with conventional methods and presumably rough. Further experiments[5, 6, 7] with mixtures of ^3He and ^4He showed that the slip was increased substantially as the concentration of ^4He was increased to correspond to surfaces covered with several monolayers of ^4He (the ^4He preferentially coats the walls), leading to change

of the scattering from diffuse to nearly completely specular[8, 9]. The addition of the ^4He suggests that it acted to smooth the rough surfaces, i.e. the diffuse scattering was due to the geometric roughness of the boundaries.

In our experiment we used an Andronikashvili type torsional oscillator to measure the properties of a thin slab of ^3He. The fluid was constrained in a cell with depth of $640\,nm$ and diameter $1\,cm$ which had one surface made out of highly polished glass and the other of crystalline silicon. The cell was designed to withstand pressurization of at least 50 psi.

Our measurements for the normal ^3He showed that the fluid experienced considerable slip over the temperature range we conducted the experiment. At $160\,mK$ we observed only half of the fluid to be coupled with the oscillator, and at temperatures bellow $100\,mK$ the fluid was completely decoupled from the oscillator. This was compared with the results of an experiment conducted by Casey[10] with a somewhat different surface roughness of the boundary.

Since the slip of the normal ^3He fluid masked the signal of the superfluid we were unable to observe the phase transitions of the constrained helium. Nevertheless the behavior of superfluid ^3He in thin films is described in the next section as the study of the superfluid was the original motivation to build the current experiment. In addition there are indications[11] that the surfaces of the current experiment can be modified to observe the phase transitions of the superfluid ^3He.

1.2 The effect of walls on confined superfluid ^3He

Soon after Bardeen, Cooper and Schriefer proposed their theory of superconductivity in metals[12], the Cooper pairing mechanism began to be studied in other fermionic systems such as ^3He. In contrast to the electrons in metals, which form pairs with zero angular momentum, the ^3He pairs have nonzero angular momentum due to the strong hard-core repulsion. This leads to an anisotropic wave function for the pairs, and thus to the anisotropic properties of the superfluid ^3He.

Superfluid ^3He has proven an excellent model for testing the limits of the BCS theory. The study of the bulk ^3He has led to good understanding of the A and B phases. In thin films it is the only model system besides ultrathin superconducting films where two dimensional Fermi superfluidity/superconductivity can be tested.

The pressure, temperature, geometry and magnetic fields affect which of the phases (A or B) is stable and has the lower energy at given parameters. The distance at which it is energetically unfavorable to vary the order parameter is given by the coherence length from the Ginzburg-Landau theory:

$$\xi(T) = \sqrt{\frac{3}{5}} \frac{\xi_0}{\sqrt{1 - \frac{T}{T_C}}} \tag{1.1}$$

where the spatial extension of the Cooper pair is characterized by the zero temperature coherence length:

$$\xi_0 = \frac{\hbar v_F}{2\pi k_B T_C} \tag{1.2}$$

Greywall[1] has determined the zero temperature coherence length ξ_0 as a

function of the pressure (figure 1.1) and determined that it can be varied from 87.8*nm* at zero pressure to 17.7*nm* at the solidification pressure.

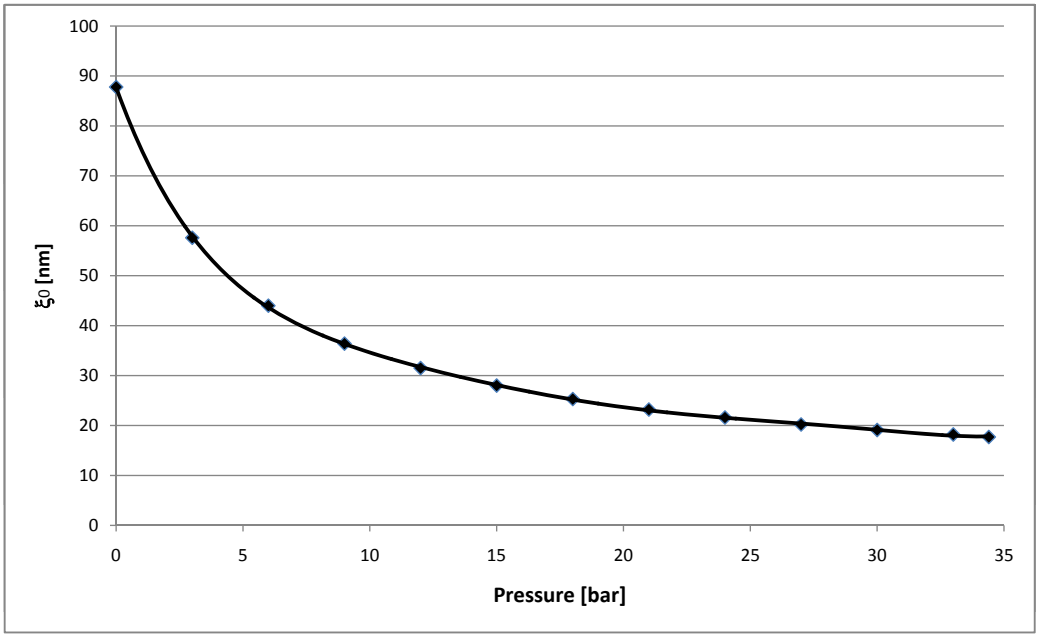

Figure 1.1: Zero temperature coherence length ξ_0 as a function of pressure (after Greywall 1986[1]).

The wide range of variation of ξ_0 under pressure allows the dimensionless length D/ξ_0 to be changed considerably without modifying the spacing D between the walls of the cell. The range of D/ξ_0 accessible for our cell is $\gtrsim 7.3$ and is to the right of the solid line in figure 1.5.

For thin films of superfluid ^3He with thickness D that are of the order of

the coherence length $D \sim \xi(T)$ the films are said to be two-dimensional and are expected to display different behavior from bulk superfluid ^3He.

Theoretical work by Li and Ho[17] explored the phase diagram of ^3He in constrained geometries. The boundaries of the slab act to pin the orbital part of the order parameter and promote the A phase near T_C. Further, the A phase becomes unstable to a deformed B phase as the temperature is lowered. From equation 1.1 and the condition $D \sim \xi(T)$ it is seen that the promotion of the A phase will occur over wider region of temperatures as the thickness of the slab is decreased. The phase diagrams of the ^3He for diffusely and specularly scattering boundaries in constrained slabs as calculated by Li and Ho are given in figures 1.2 and 1.3.

In addition, Vorontsov and Sauls[19] have calculated the spatial profile of the order parameter components for both the B and A phases of the superfluid ^3He (figure 1.4) constrained by boundaries that reflect the quaisparticles either both specularly (dashed line) or one diffusely and the other specularly (solid line). The perpendicular component of the order parameter of the B phase is suppressed for both scattering conditions and the parallel component is not suppressed when both surfaces scatter specularly. For the A phase the perpendicular component of the order parameter is always zero due to the aligning of the pair angular momentum along the energy gap axis.

Theoretical works by Nagato and Nagai[20] and Vorontsov and Sauls[19] predict phase transition for the confined helium when the film thickness is of the order of $10\xi_0$ (figure 1.5). An interesting feature of the A-B transition appears when $T/T_C \approx 0.4$. For example if a film with thickness $D = 9.4\xi_0$ is constrained by a diffusely scattering surface, as it is cooled a phase transition from the A to

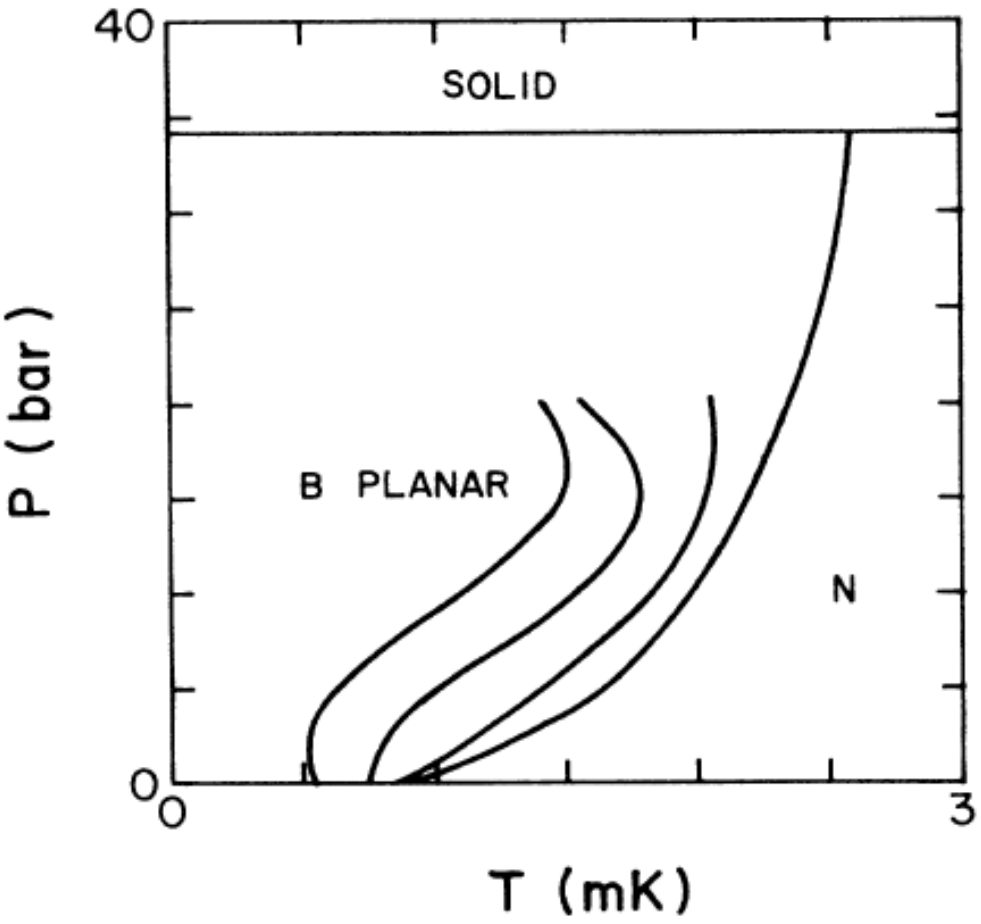

Figure 1.2: The phase diagram between the A and B-planar phases for diffusely scattering boundaries. The lines from left to right correspond to $D = 200nm$, $D = 300nm$, $D = 500nm$ and bulk (after Li and Ho[17]).

B phase occurs at temperature $T_{AB} \approx 0.55T_C$. As the temperature is decreased further the A phase is reentrant and the B to A phase boundary is crossed at temperature $T_{AB} \approx 0.23T_C$.

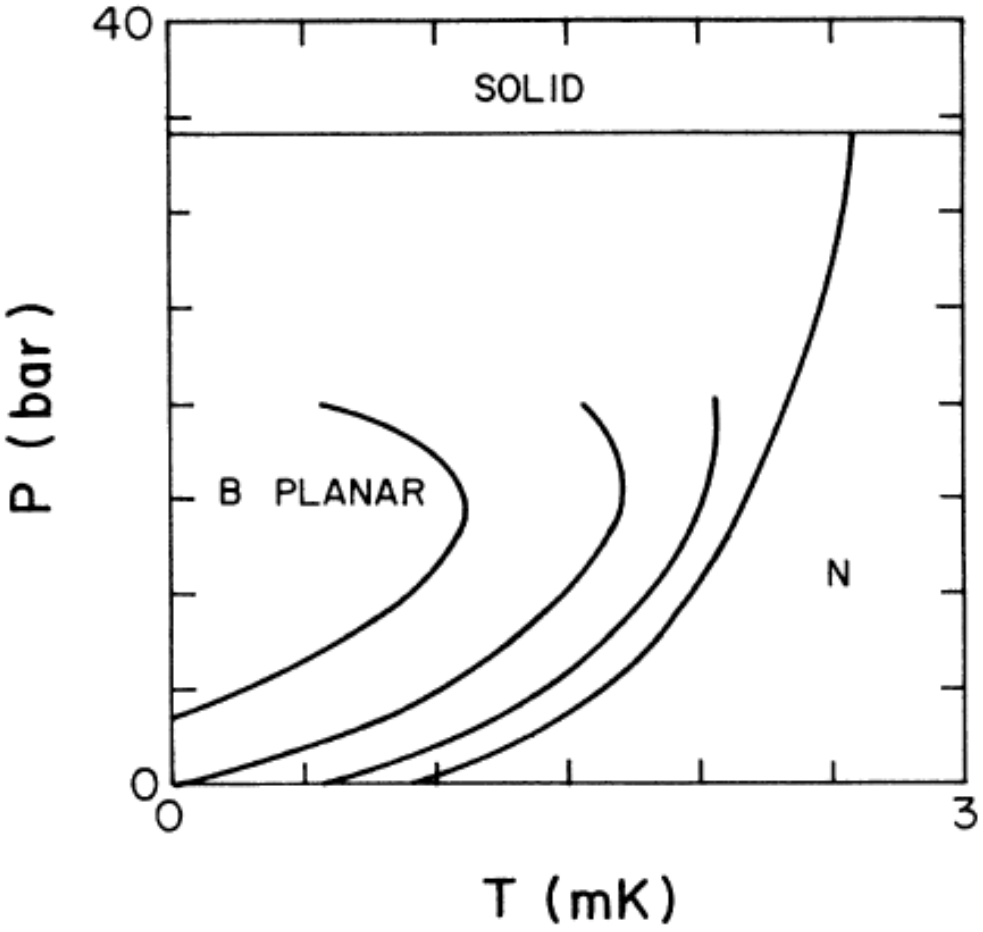

Figure 1.3: The phase diagram between the A and B-planar phases for specularly scattering boundaries. The lines from left to right correspond to $D = 200nm$, $D = 300nm$, $D = 500nm$ and bulk (after Li and Ho[17]).

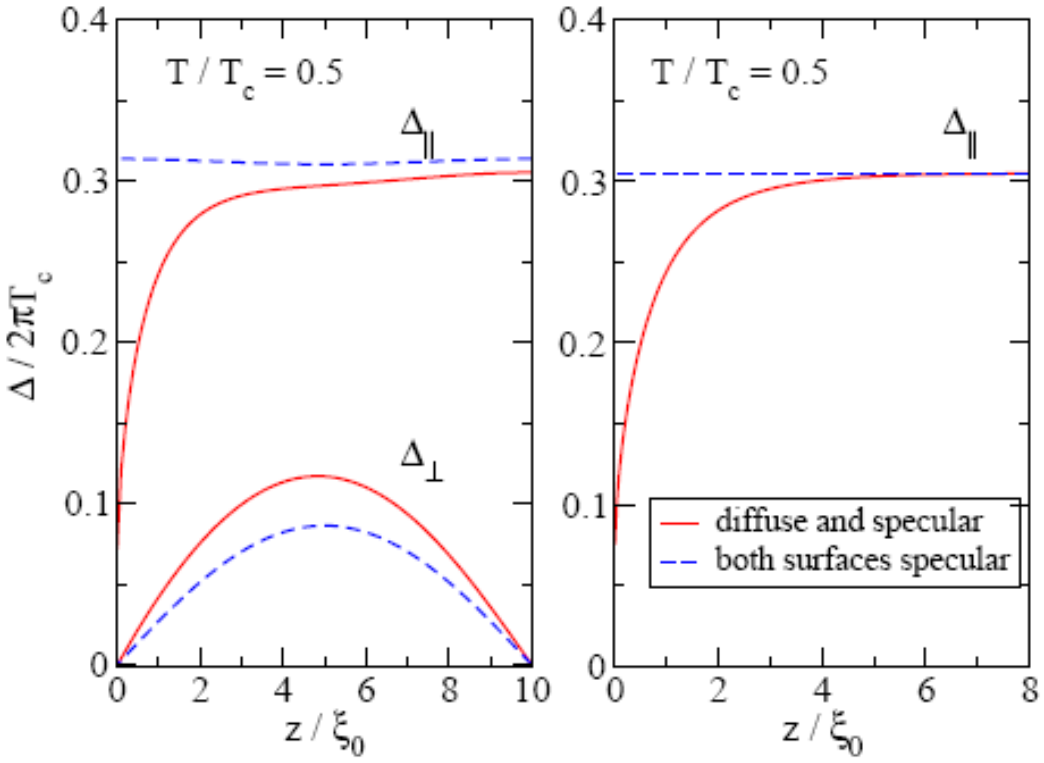

Figure 1.4: The order parameter of the B-phase (left) and the A-phase (right) in thin film of ^3He (after Vorontsov[19]).

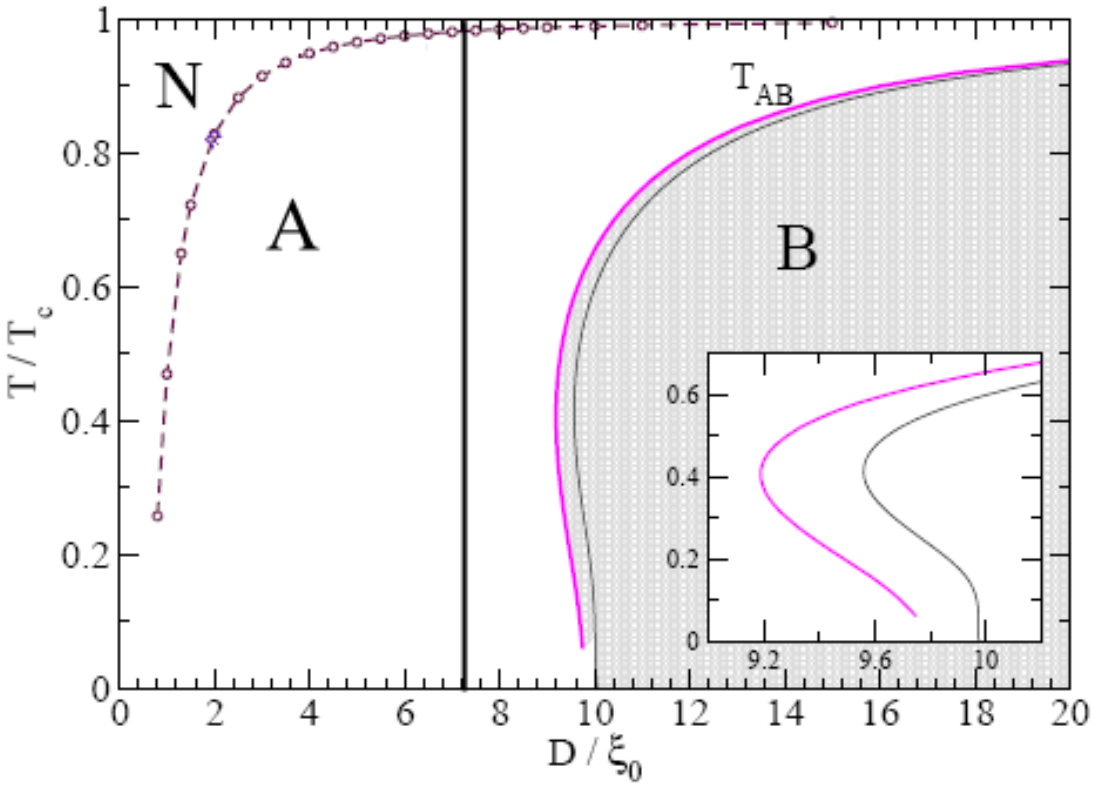

Figure 1.5: Phase diagram for the superfluid ^3He films. The thin black line is for the A-B transition of specular-diffuse scattering and the purple line is the A-B transition of film with specular-specular scattering at the surfaces. The inset shows the enlarged portion of the reentrant region. The dashed line shows the Normal to A transition with suppression of the transition due to diffuse scattering by the boundaries. Our experiment was designed to be sensitive to the region on the right of the solid line (after Vorontsov[19]).

1.3 Outline

Superfluid ^3He can be modelled as a mixture of two interpenetrating fluids: one normal and the other superfluid with respective densities ρ_n and ρ_s the total density of the fluid being $\rho = \rho_n + \rho_s$. In the bulk case the superfluid fraction ρ_s/ρ is a function of the reduced temperature T/T_C but the superfluid fraction may be modified in the case of thin films. In the bulk ^3He the transition between the A and B phases provides a discontinuous change in the superfluid density[18] which an experiment could detect.

CHAPTER 2

MAKING THE OSCILLATOR

In this chapter we describe the technology to make the torsional oscillator, the challenges that we encountered during the fabrication and assembly, and the way we solved them.

The head of the oscillator contains a microcavity and was manufactured mainly with the equipment at the ”Cornell NanoScale Science and Technology Facility” (CNF). The fill line of the cell and its sizing to the proper dimensions was made with equipment of the ”Cornell Center for Material Research” (CCMR). The mechanical parts of the oscillator were also manufactured at the LASSP machine shop.

A particular challenge encountered while making the cell was the collapse of the cavity during the anodic bonding of the silicon and glass. This was rather surprising as the theory[13] predicted that for the dimensions of our cavity, no collapse should occur. The problem was solved by modifying the electrodes for the bonding equipment as described in chapter 2.1.10.

2.1 Making the cell

To conduct the experiment on thin films of ^3He we devised a cavity with depth of $640nm$ and width of up to $1cm$. To achieve such a high aspect ratios for the width versus depth of the cavity we used micro fabrication and lithography on a single crystal silicon that was capped with anodically bonded glass. The silicon crystal has $< 100 >$ orientation.

The process flow for making the head of the torsional cell is given on fig. 2.1 and involves the following steps (details of each step are given later in this chapter):

1. Depositing $4\mu m\ SiO_2$ using PECVD (if the wafer does not have initial thermal oxide).
2. Depositing photoresist and patterning the wafer. Developing the photoresist.
3. Etching the oxide over the developed photoresist in HF. Stripping the remaining photoresist.
4. Thermal oxidation of the wafer.
5. Drilling the fill line hole. Sizing the silicon pieces to their final dimensions.
6. Cleaning the silicon. Etching the remaining oxide.
7. Anodic bonding of silicon and glass. Formation of the cavity.
8. Sizing the glass to match the dimensions of the silicon. Cleaning up residual contaminants.

The thickness of the silicon and glass wafers is $3mm$ each which is considerable thicker than the standard wafers used for lithographic processing and anodic bonding ($300\mu m$). We used such wafers in order to minimize the bending of the wafers and the change of the cavity depth when the experiment is pressurized.

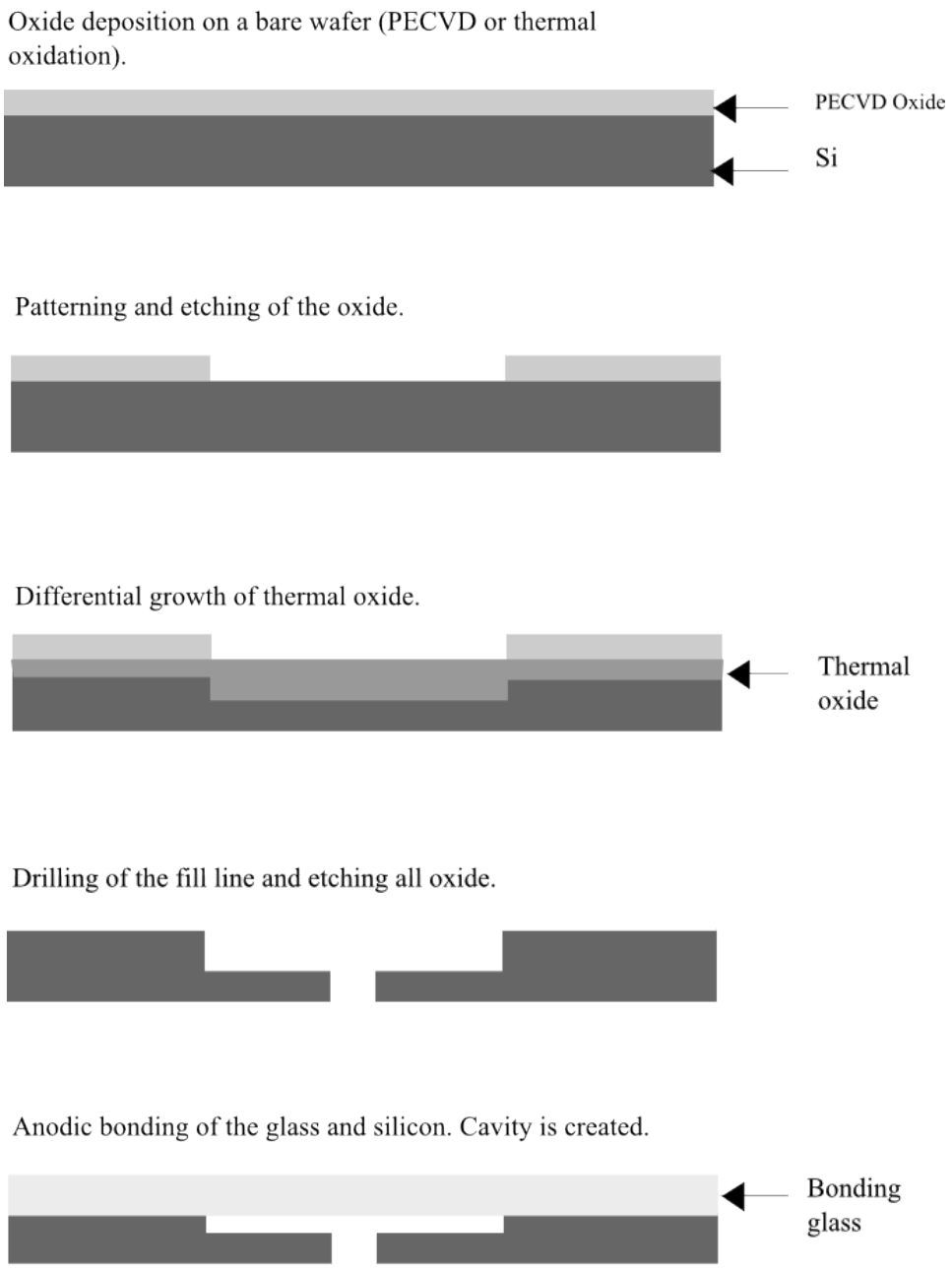

Figure 2.1: Process flow for making the cavity.

2.1.1 Cavity design and mask production

We have developed three different design patterns for the cells. One of the patterns consists of differently sized rectangular cavities (fig. 2.2) to be used both for the study of the anodic bonding collapse problem and for an experiment to study the properties of the two dimensional superfluid ^3He with NMR[22]. The other two patterns (fig. 2.3) are for circular cavities to be used for the torsional oscillator experiment described in this work. We managed to solve the collapse problem for both types of circular cavities but decided to use the doughnut shaped ones (shown in the lower part of figure 2.3) in order to increase their survival chance when cooled to helium temperatures in the cryostat.

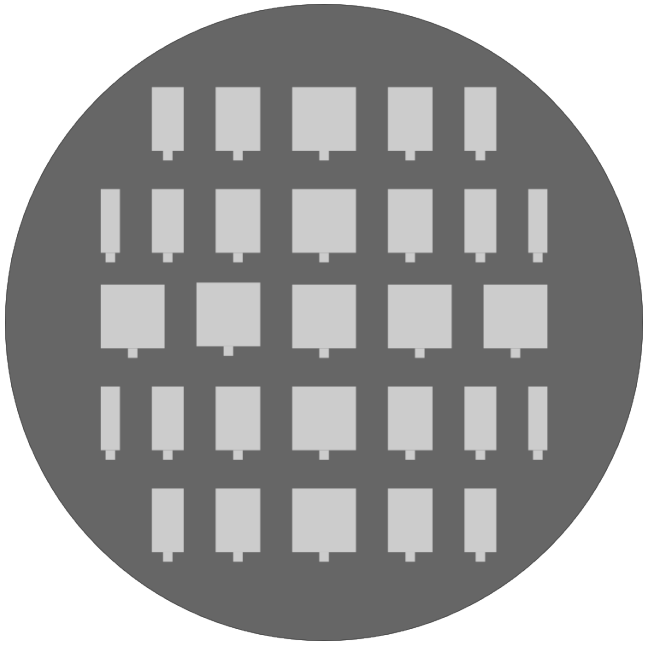

Figure 2.2: Pattern for studying the anodic bonding collapse problem.

The design for the cavities was done with the layout editing software L-Edit. The files were then transferred to *GCA/MANN 3600F Optical Pattern Generator* and the corresponding patterns printed on blank chrome masks.

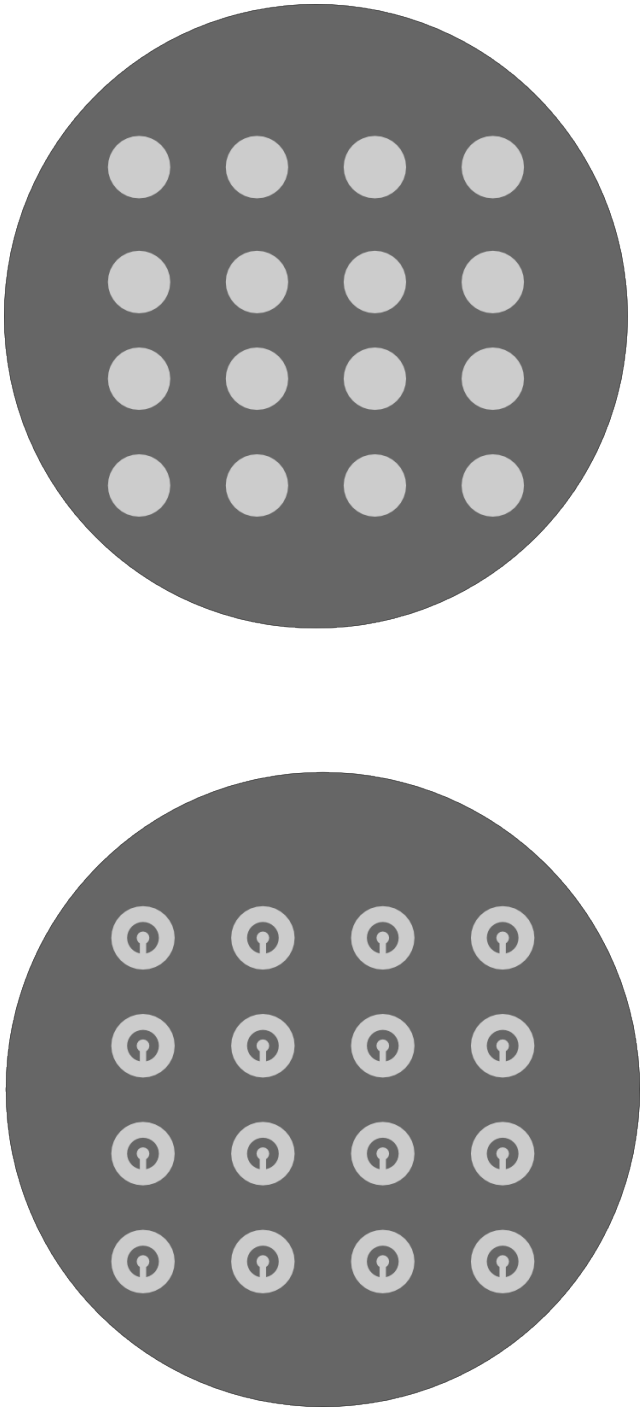

Figure 2.3: Patterns for the torsional oscillator experiment described in this work. The top pattern was used to optimize the production of the cavities and the lower is used for the head of the oscillator.

2.1.2 Deposition of first oxide layer

For the creation of the step of the cavities we have used differential growth of the thermally oxidized wafers. To achieve this an initial layer of oxide is required to be deposited on the wafer. While we ended using wafers with commercially grown thermal oxide with thickness $2.7\mu m$ which we increased to $4\mu m$ using plasma enhanced chemical vapor deposition a big part of our tests were done on wafers without the initial oxide. In this section we briefly describe the procedure to deposit the first layer of SiO_2.

The first oxide layer can be either grown through thermal oxidation or chemical vapor deposition. The thermal oxidation does provide better uniformity of the oxide thickness over the whole wafer but to achieve the required thickness of approximately $4\mu m$ requires about 31 hours of processing. A faster and cheaper method is to use the available *"IPE 1000"* plasma enhanced CVD chamber. To obtain the SiO_2 layer we employ the reaction of SiH_4 and N_2O gases[16]. The parameters used for the deposition process are given in table 2.1.

Table 2.1: Parameters used for the PECVD deposition

Temperature	$275°C$
Silane (SiH_4)	$6sccm$
Nitrous Oxide (N_2O)	$54sccm$
Pressure	$450mtorr$
Power to the plasma	$44W$
Deposition rate	$40 - 42nm/min$

We have run the above recipe in four 25 minute phases to obtain the $3\mu m$ oxide film. The process is interrupted so that the chamber is cleaned and the precipitate formed on the chamber walls is removed. If the chamber is not cleaned on time the precipitate begins to ″snow″ on the wafer and the oxide layer has inferior quality. After 100 minutes of deposition we measured the thickness of the oxide to be slowly varying between $3770 - 4210nm$ across the wafer.

As the variation of the oxide thickness is generally linear over the whole wafer we can consider that at a point on the edge of the wafer the oxide will have the highest thickness and at a point diametrally opposite the oxide will be the thinnest. This variation will create a difference of $18nm$ of silicon consumed end to end on the wafer (more details in section 2.1.4). Since the diameter of the cell is 1/10 of the diameter of the wafer we will expect to see variation of the cavity depth of no more than $2nm$.

2.1.3 Patterning the wafer

With the first layer of oxide deposited on the wafer we proceed to patterning the cavities. First photoresist is spun on the wafer and baked on a hotplate at $90°C$ for a minute. With the resist hardened, the wafer and the pattern mask are placed in the *ABM High Resolution Mask Aligner*. The mask is then irradiated with $254nm$ UV light for 20 seconds. The light that is not shielded by the mask chemically alters the resist and prepares it for developing.

After the exposure to UV light the silicon wafer is immersed in photo developer solution to dissolve the resist that has been exposed. The wafer is then rinsed in deionized water and blown dry with nitrogen. Next the wafer is im-

mersed in buffered oxide etch with concentration of 6 : 1 (BOE 6:1). The BOE dissolves the oxide on the wafer that is not protected by resist and the etch stops when the bare silicon is reached. When the etching is complete the wafer is rinsed in DI water followed by a bath of solvents (combination of propylene glycol, N-Methylpyrrolidone and Tetramethylammonium Hydroxide) heated to $70^{\circ}C$ to remove the unexposed resist.

2.1.4 Step creation for the cavities

After the patterning of the cavities is done we have a wafer covered with about $4\mu m\ SiO_2$ with bare silicon exposed at the future location of the cavities. To create the steps for the cavities we employ a differential growth method of the thermal oxide: more silicon is consumed for a given elapsed time if the initial oxide layer is thinner compared to thicker initial layer. The Deal-Grove model[21] is a good description for the differential growth.

Deal-Grove model

The Deal-Grove model considers the oxidation to occur at the interface between the oxide and the substrate. Thus the model incorporates three different and distinct phenomena that the oxidizing species undergo (fig. 2.4):

1. Transport of the oxidant species from the bulk of the oxidizing gas to the outer surface of the wafer where they are absorbed.
2. Diffusion of the oxidizing species through the existing oxide layer towards the silicon surface.

3. Reaction of the oxidizing species with the silicon at its surface and the formation of increased thickness of SiO_2.

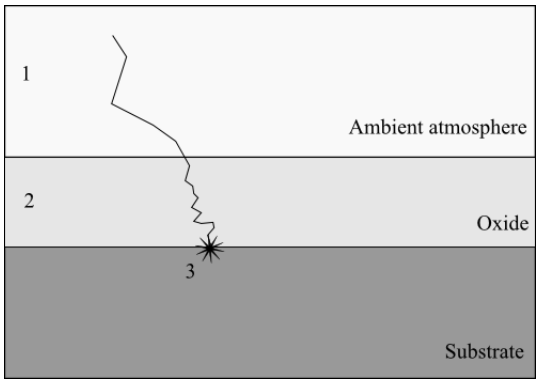

Figure 2.4: Schematic of the path of the oxidizing species for the Deal-Grove model processes.

The model assumes steady state conditions for which the rate with which the three stages listed above progress is proportional to the concentration of the oxidant species. Therefore the first case is governed by the Henry's law, the second by the Fick's law of diffusion, and the third by a first-order reaction with respect to the oxidizing species. Setting the oxygen flow rates of the three cases to be equal to one another we find that the growth rate is determined from the oxidant reaction flux with the crystalline silicon. Usually the first stage does not limit the reaction rate and is dropped for simplification. Therefore the oxide thickness X_0 on initially bare substrate can be found as a function of oxidation time t:

$$t = \frac{X_0^2}{B} + \frac{X_0}{B/A} \tag{2.1}$$

where the constant A is determined from the reaction properties and B is determined by the thickness of the oxide layer. This equation is used to determine

the oxide thickness over the cavity pattern.

Outside the pattern of the cavities we have preexistent oxide. To take its growth into account, the time τ necessary for the initial thickness of the layer to be grown is considered. Therefore outside the cavity patterns the oxide thickness can be determined from:

$$X_0(t) = \frac{A}{2}\left(\sqrt{1 + \frac{4B}{A^2}(t+\tau)} - 1\right) \tag{2.2}$$

From the discriminant it is observed that there are two regimes for the growth of the oxide:

$$\begin{aligned} t + \tau \ll \frac{A^2}{4B} &\Rightarrow X_0(t) = \frac{B}{A}(t+\tau) \\ t + \tau \gg \frac{A^2}{4B} &\Rightarrow X_0(t) = \sqrt{B(t+\tau)} \end{aligned} \tag{2.3}$$

The quadratic parameter B and the linear parameter B/A are dependent on the temperature of oxidation as follows:

$$\begin{aligned} B/A &= (B/A)_0 e^{-E_1/kT} \\ B &= B_0 e^{-E_2/kT} \end{aligned} \tag{2.4}$$

where E_1 and E_2 are the corresponding activation energies for the linear and parabolic terms, and k is the Boltzmann constant.

The activation energies and the linear and parabolic constants are dependent on many factors and are usually determined experimentally. Table 2.2 gives the empirical values for the growth of oxide on low doped single crystal silicon at

Table 2.2: Parameters used for the calculation of the oxide thickness.

Parameter	Quantity	Wet (H_2O)	Dry (O_2)
Linear constant	$(B/A)_0$	$< 100 >: 9.7 \cdot 10^7 \mu m/hr$ $< 111 >: 1.63 \cdot 10^8 \mu m/hr$	$< 100 >: 3.71 \cdot 10^6 \mu m/hr$ $< 111 >: 6.23 \cdot 10^6 \mu m/hr$
	E_1	$2.05eV$	$2.00eV$
Parabolic constant	B_0	$386 \mu m^2/hr$	$772 \mu m^2/hr$
	E_2	$0.78eV$	$1.23eV$

atmospheric pressure. These parameters correspond to the conditions that we used for the thermal oxidation.

Studies by Deal and Sklar[26] reveal that silicon heavily doped with phosphorus (concentration between $4 \cdot 10^{15} - 1.5 \cdot 10^{20} cm^{-3}$) will not experience appreciable change of the rate of oxidation for temperatures between $1000 - 1200C$ as compared to low doped silicon. This ensures that the level of doping for the wafers that we use does not affect the oxide growth rate.

Figure 2.5 shows the thickness of oxide as a function of time on a silicon wafer with $< 100 >$ orientation at $1100°C$ when processed in wet atmosphere ($\approx$ 95% H_2O gas) at $1atm$ pressure. This graph is consistent with the process conditions that we used.

It should be noted that the Deal-Grove model is not well suited for determining the growth rate of the first $\approx 30nm$ of the SiO_2. Since we deal with much thicker oxide layers the discrepancy of the time needed to complete the oxidation is negligible.

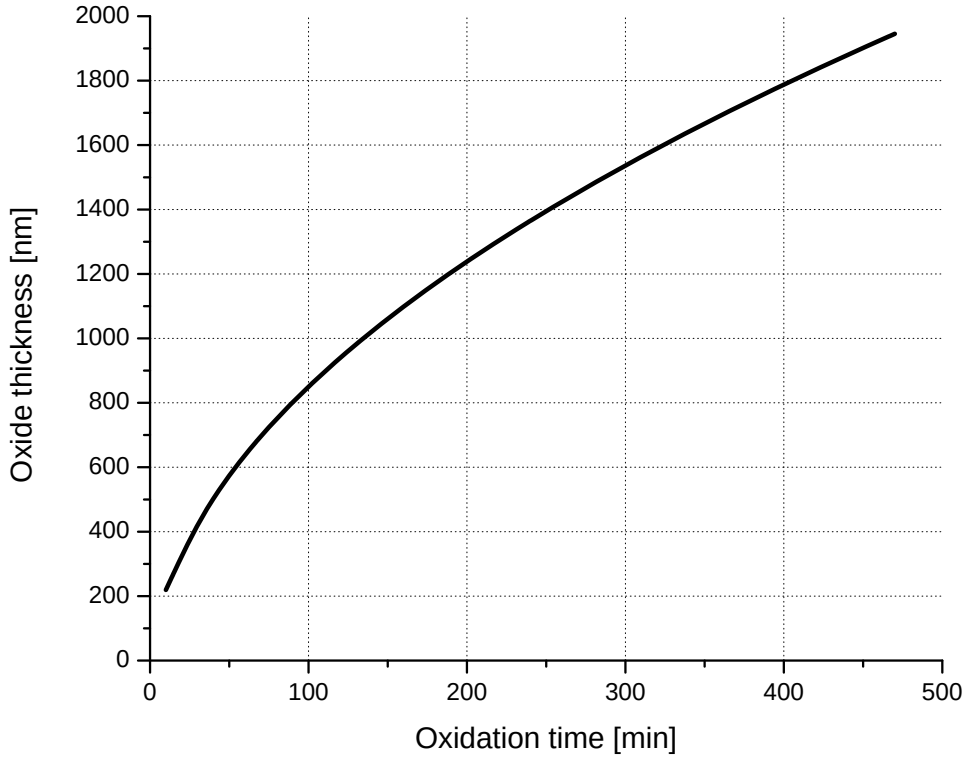

Figure 2.5: Thermal oxide growth as a function of time.

Silicon expansion

Since the gap of the cavity in the silicon is created by the consumption of the silicon during the oxidation we have to consider the change of the lattice structure during this process.

As the oxygen atoms diffuse into the silicon they disrupt the $Si - Si$ bonds and create $Si - O$ bonds. To understand the expansion of the silicon we consider that for the crystalline silicon the volume allocated to a single silicon atom is 20.0Å^3 and for SiO_2 the volume is 44.5Å^3. It is considered that during the

expansion process the silicon atoms remain in their atomic plane and merely increase their interatomic distances in direction of the surface. Thus the new unit cell of the SiO_2 will have dimensions in the growth direction 44.5/20.0 = 2.2 times that of the crystalline silicon. So for every μm of silicon consumed $2.2\mu m$ of SiO_2 will be grown.

Combining the Deal-Grove model with the expansion of the lattice structure of the silicon gives the necessary tools to calculate the time for the oxidation.

Oxidation procedure

Before loading the wafers for thermal oxidation in the furnace they have to be thoroughly cleaned from impurities in the MOS hoods. The first step removes the organic contaminants using automated $RC-1$ clean (description of the chemical composition for this cleaning step is given in chapter 2.1.9). After the wafers are rinsed in deionized water they are subjected to automated $RC-2$ clean with $1:1:6$ solution of $H_2O_2 : HCl : H_2O$ heated to $80°C$ to remove metallic contaminants. After the wafers are rinsed in DI water and dried off with nitrogen they are loaded in the thermal oxidation furnace.

We have run the oxidation process at the parameters giving the fastest SiO_2 growth rate for the equipment. The oxidation is done in wet atmosphere at $1100°C$ for 420 minutes. The oxide thickness over the patterned region and over the remaining initial layer after the oxidation is complete is given in the table below:

With the so processed wafers we observe that the silicon consumed under the patterned regions is $640nm$ more than the areas with the primary oxide.

Table 2.3: Thermal oxidation of the wafer

Initial SiO_2 thickness	Final SiO_2 thickness	Additional SiO_2 grown Additional SiO_2 grown	Consumed Si Consumed Si
$0nm$	$1834nm$	$1834nm$	$834nm$
$4000nm$	$4430nm$	$443nm$	$195nm$

After stripping all the oxide this difference becomes the basis for the cavities. At later stage of the cavity production we measure the depths to be between $625nm - 647nm$.

2.1.5 Drilling the fill line hole

With the thermal oxidation complete, the next step of making the cell is to drill a hole for mounting the cell on the torsional rod. The torsional rod also supplies the helium for the experiment. The profile (that we attempted to achieve) of the hole is as shown in figure 2.6A. The step in the profile is necessary to prevent any epoxy entering in the formed cavity when the cell is mounted on the torsional rod.

When we were planning the experiment we expected to use the deep reactive ion etch (DRIE) machine available at CNF for making the fill line in the silicon. The DRIE would have provided excellent quality holes with vertical walls and no damage at the entry and exit points of the holes. Unfortunately the thickness of the silicon wafers (3mm) is greater than what the machine is currently calibrated to handle and we were not permitted to use it. While it is possible

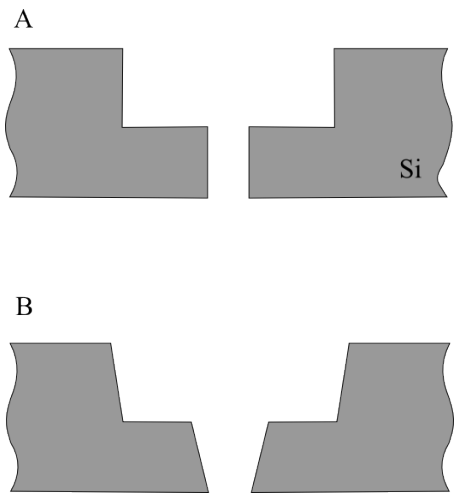

Figure 2.6: A: Attempted profile of the fill line hole. Achievable by DRIE and laser drilling for thin wafers. B: Profile as achieved with ultrasonic mill. The deviation from the vertical is $2^\circ - 5^\circ$.

to recalibrate the DRIE for thick wafers, the staff refused to do so as this is one of the more heavily used instruments at CNF and would have affected many users.

Without the option of using the DRIE we resorted to use ultrasonic drilling and (attempted) laser drilling outside the clean room. With the oxide layer still present on the silicon wafer (kept to reduce the amount of scratching of the wafer surface while handled outside the clean room) we proceed to drill the fill line.

Marking the back of the wafer

As the profile of the hole for the fill line suggests, the drilling has to be done in two steps. In our case we first drill the hole with the smaller diameter through the whole wafer, followed by a larger hole to the desired depth.

The pattern on the wafer is easily seen and we could have used it to position the small drill and make the hole from the patterned side towards the back of the wafer and followed up by using the exit hole on the back to guide the thicker drill. We chose not to drill from the front of the wafer as the holes drilled with our equipment tended to be slightly conical with the wider side at the entry position of the drill(fig. 2.6B). The walls deviate $2 - 5$ degrees from the vertical.

To transfer the exact position of the holes to the back of the wafer we made a contraption as shown on figure 2.7. We have two plates made of transparent lucite that are clamped together while they were machined. Using the milling machine we drill through both plates with drill number 75 pattern corresponding to the position of the holes on the wafer. In addition we drill 6 more holes with $1/4$ inch drill to be used for alignment and clamping the wafer when inserted. In 3 of the larger holes we put precision steel rods to restrict the movement of the plates with respect to each other. The rods allow only vertical translation of the plates and the small holes are kept well aligned. In the remaining large holes we insert a $1/4$ inch bolt with a winged nut at the other end to clamp the wafer when inserted. With the so prepared contraption we position the silicon wafer on the lower lucite plate with the patterned side facing up. Then we put the second lucite plate and press it against the wafer. The silicon wafer is then aligned so that the positions to be drilled is visible through the small holes of the upper lucite plate. When the alignment is good the winged nuts are tightened and the whole stack is turned with the back of the silicon wafer facing up.

With pliers we carefully extract the tip of a 0.5mm permanent marker and insert it in the lucite plate so that it touches and marks the back of the wafer. After taking the tip out of the hole it is inserted back into the marker to soak

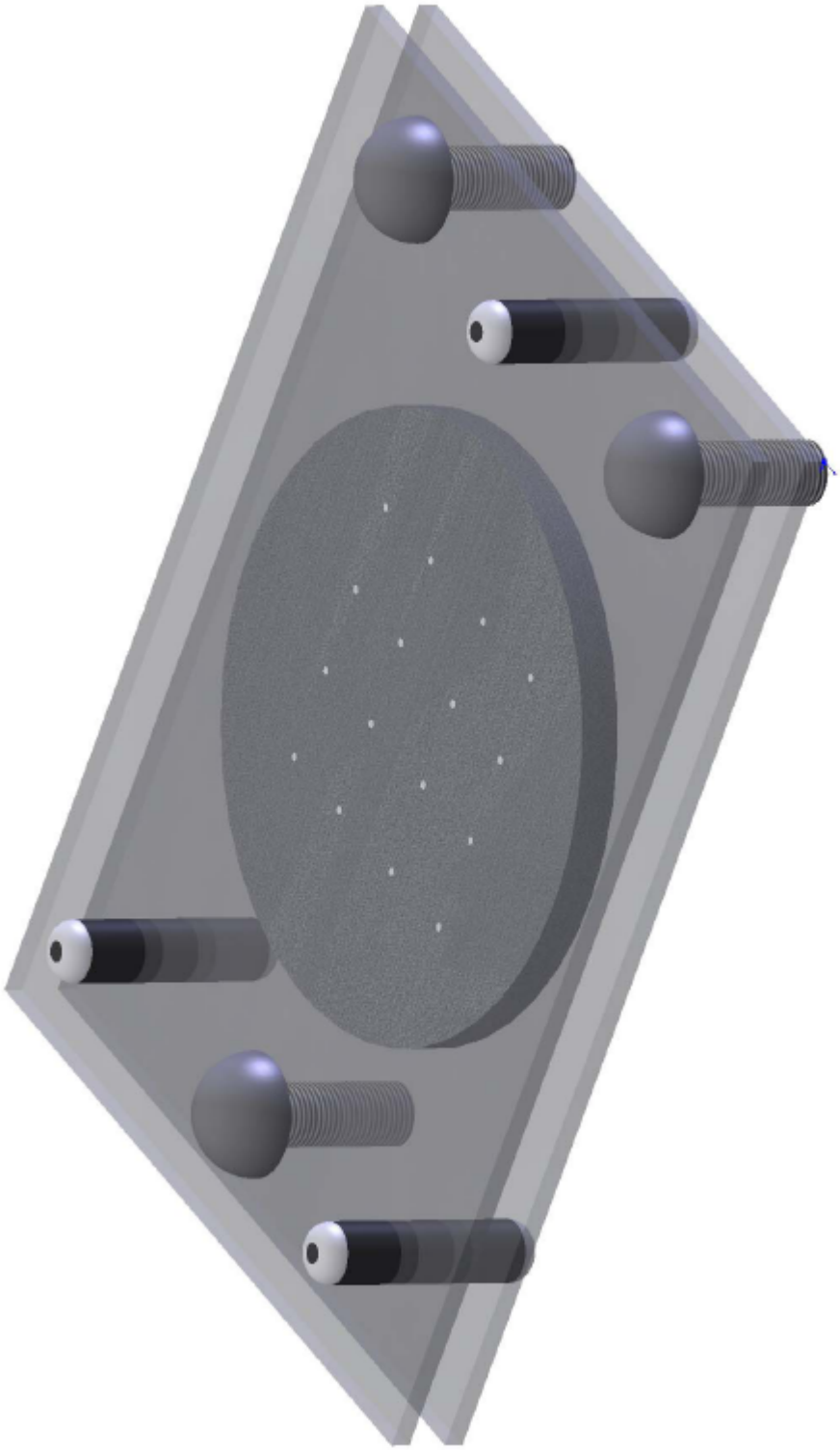

Figure 2.7: Contraption for translating the position of the hole positions.

more ink and the procedure is repeated until all of the holes are marked. The so prepared wafer is taken out of the contraption and is ready for drilling.

Ultrasonic mill

The ultrasonic drilling is done by exciting abrasive powder over the required region of the wafer by sound waves. Schematics of the sonic mill is given in figure 2.8. The frame supports an electromagnet holder, pneumatic system, and dispensing system for supplying the abrasive slurry.

The pneumatic system controls the height of the drill bit. It is set to have downward motion of 0.5mm per minute interrupted every 30 seconds by rapidly raising the drill bit above the surface of the wafer. This is required to allow the waste products of the drilling to be flushed out and fresh slurry to enter the hole. After 5 seconds pause the drill bit is lowered again to its last position and the drilling is continued. This cycle is repeated until the smaller drill bit is 3.5mm below the surface of the wafer. The additional 0.5mm are necessary to take into account the wearing out of the drill bit from the abrasive grains. With the bigger drill bit the cycle is repeated until the bit is about 1.5mm below the surface of the wafer (approximately halfway through the wafer).

The dispensing system continuously supplies abrasive slurry over the region where the drilling is performed. The slurry flow can be controlled by squeezing the supply hose with a varying width clamp. While too much slurry does not affect adversely the drilling process, the drainage system may be burdened and slurry can spill out of the machine. The drainage returns the slurry to the storage tank for recirculation. The slurry is a fine powder of silicon carbide dispersed in

water. To prevent sedimentation of the powder in the storage reservoir constant circulation is needed.

The ultrasonic transducer is directly connected to the pneumatic system of the sonic mill. The frequency of the transducer can be varied to optimize the drilling. At 20 KHz we obtained the best possible profile of the hole. The sound waves are propagated to the wafer by a hardened steel bit coupled to the transducer.

To make the drill bit we use a blank 1/2"-20 threads per inch bolt with a hexagonal head. With the bolt mounted in a lathe we choose a standard drill bit which has a shaft diameter equal to the diameter of the hole we need. The drill bit is held with a finger chuck and used to bore 1-1.5cm into the center of the bolt. After that the threaded part of the drill is cut, the bored hole is thoroughly cleaned using soapy water followed by isopropanol rinsing and the remaining shaft of the bit is hard-soldered into the drilled bolt. Special attention must be paid that the protruding part of the drill bit is perpendicular to the face of the bolt, or the bit will break while using the ultrasonic mill. It is best to keep the length of the protruding bit to around 1cm.

When work is done on a sample with the sonic mill, the sample has to be fixed securely as the vibration will move it around and the hole produced will have a bigger diameter and may not even be circular. To do so, the silicon wafer is glued to a piece of flat glass with "Clear Bond" brand polymer, and the glass in turn is glued to an iron plate as in figure 2.10. The whole stack then is firmly held by an electromagnet positioned above the drainage system of the sonic mill.

2.1.6 Ensuring the integrity of the hole

Our initial attempts at drilling with the sonic mill were disappointing as the wafer displayed chipped exit hole (figure 2.9A). Adjustment of the parameters of the sonic mill such as sound frequency and translation rate did not improve the outcome of the drilling process. Given the results we decided to investigate laser drilling of the wafer (described in the next section). Unfortunately those attempts were also unsuccessful and once again we resorted to the ultrasonic mill after modifying the way the wafer is attached to the glass/iron plate.

In our initial attempts to use the sonic mill we applied a thin layer between the silicon wafer and the plate as directed by the instructions of the polymer. Later we decided to melt a sufficient amount of polymer to keep the silicon wafer 2*mm* above the glass and encasing it up to the upper edge (figure 2.10B). With the so prepared wafer the drilling of the fill line holes was successful as we obtained clean edges without chipping at the exit point of the drill (figure 2.9B).

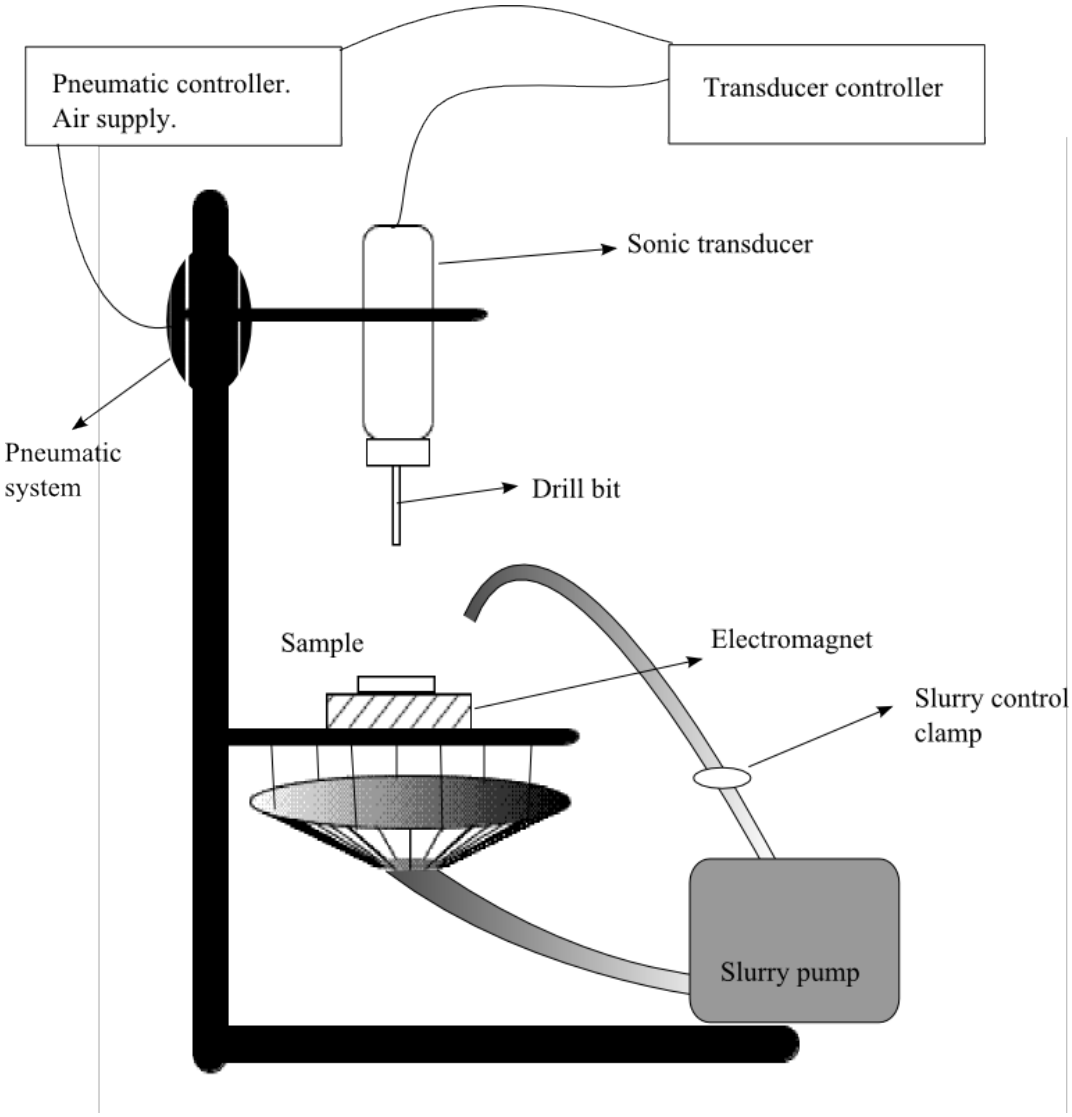

Figure 2.8: Ultrasonic mill.

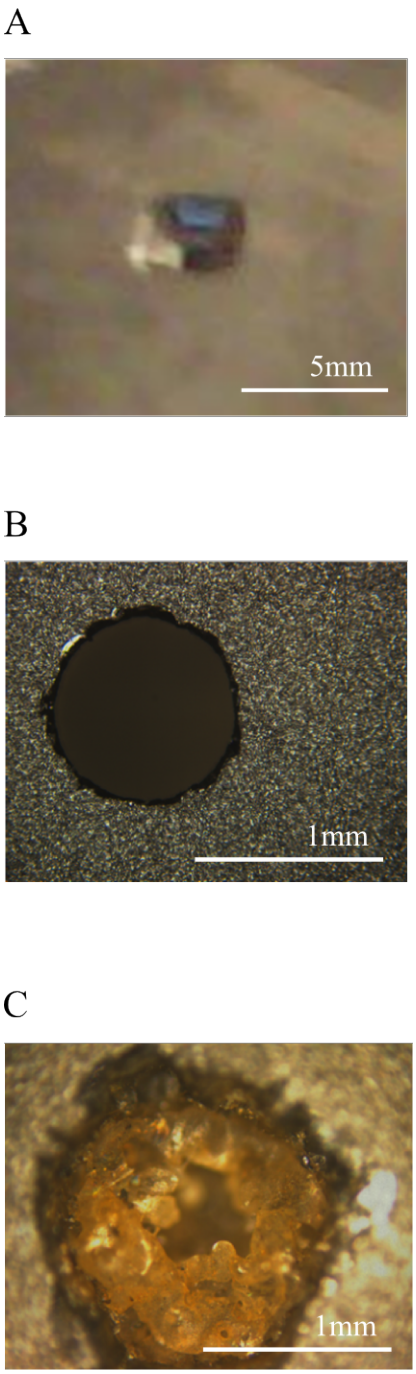

Figure 2.9: Top: exit hole after ultrasonic drilling. The sample has been attached with only thin layer of bonding agent. Middle: ultrasonic drilling with sample encased in bonding polymer. Bottom: hole as created by the laser drilling method.

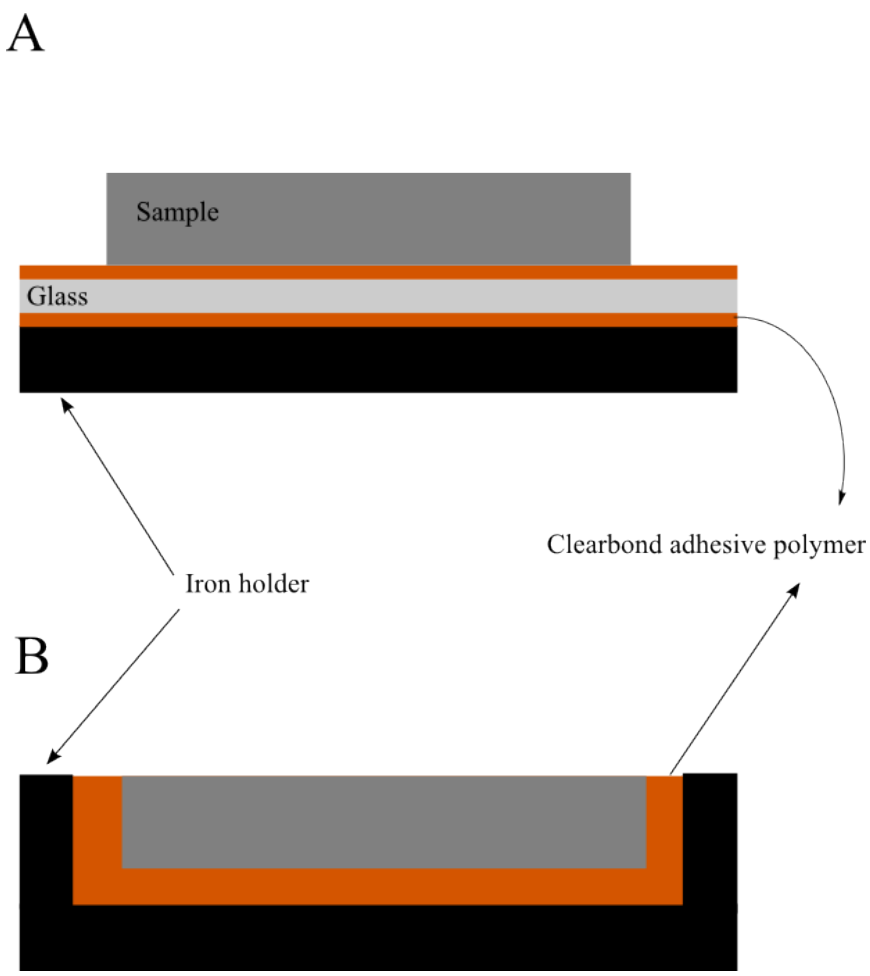

Figure 2.10: Wafer holder for the sonic mill. A: when the wafer is held with a thin layer of polymer, the holes drilled are with poor quality. B: when the wafer is encapsulated the quality of the holes improves.

2.1.7 Laser drilling

While we did not end up using the laser drilling for our cells, the process will be briefly mentioned here as it was part of our attempts to produce holes with well defined profiles. We decided to use laser drilling as we expected that the lack of pressure on the wafer would prevent chipping at the exit of the hole which we encountered for the ultrasonic drilling.

We submitted sample wafers to be laser drilled to a company specializing in laser cutting and micro-holes drilling. The sample that we initially sent were standard 4" wide, 300μm thick silicon wafers. The returned samples had holes with well defined profile and undamaged entrance and exit sides. After submitting the 3mm thick wafers, the companies contacted us that they are unable to complete the job as the wafers are being damaged from the laser (figure 2.9C).

Upon further communication with the company we determined that the discrepancy of the quality of the holes is due to the way the laser is focused on the thin and the thick wafers. In order to make the holes on the 300μm thick wafers the laser is focused to a diameter smaller than the diameter of the hole and continuously swept over the area desired to be removed. This technique allows to reduce the thermal stress on given point of the wafer. For the 3mm wafers the laser has to be kept at fixed position with respect to the wafer and thus imparting higher intensity over the illuminated region. Too high thermal stress on the silicon caused irreversible change in the surrounding silicon by producing rough and grainy surfaces (figure 2.9C).

2.1.8 Dicing the wafers

Once the fill line holes are drilled on the wafer we are ready to continue with its dicing into pieces that will be the size of the final cell. The silicon pieces have the drilled holes at their centers. While still attached to the metal holder the wafer is mounted on a saw with circular diamond blade. The saw uses a similar magnetic holder as the sonic mill. While dicing the wafer the blade is continuously sprayed with water to prevent overheating and the dispersal of fine dust.

After the silicon wafer is diced, the holder stack is placed on a hot plate to soften the bonding polymer and the pieces removed. A Hoya borosilicate wafer is then placed on the holder stack and glued in place of the silicon pieces. The borosilicate glass is then diced with the circular saw to pieces similar to the silicon ones but with sides $2mm$ longer. We need a little bit bigger glass piece to ensure that the entire surface of the silicon piece will be covered during the anodic bonding. The difference between the size of the silicon and the glass is minimized after the bonding is complete by cutting away the excess borosilicate glass.

2.1.9 Cleaning of the pieces

Having created the pieces for the cavity we need to clean them thoroughly from all residue of the bonding agent and the remaining protective oxide. Should there be any contaminants left, the subsequent anodic bonding would not be uniform and the created cell will not be leak tight.

The first step in the cleaning is used to remove the bulk of the bonding polymer. Both silicon and glass pieces are immersed in a bath of acetone and sonicated for 20 minutes. While this procedure dissolves the majority of the bonding polymer, once the pieces are taken out of the bath and the acetone evaporates, a thin layer of contamination can be observed on the surfaces.

The second cleaning step is aimed to remove the residual organic contaminants left after the acetone bath. This involves the use of *RCA SC-1* clean recipe. To prepare the recipe we mix deionized water, hydrogen peroxide and ammonium hydroxide with ratios of $H_2O : H_2O_2 : NH_4OH = 5 : 1 : 1$, and heat the mixture to $80C^{\circ}$. The silicon and glass pieces are immersed in the hot mixture for 30 minutes. After the RCA clean, the pieces are rinsed in deionized water and blown dry with nitrogen.

Since we kept the thermal oxide on the silicon wafer for protection we need to remove it before the anodic bonding. Immersion of the silicon pieces in BOE 6:1 strips the oxide. We have silicon pieces ready for bonding after they are rinsed in deionized water and dried off with nitrogen.

After the oxide is stripped we check the step heights for the cavities using *Tencor P10* profilometer. Depending on the positions of the cavities on the wafer during the oxidation processes the depths vary in between $625nm - 647nm$ for different cavities. For a single cavity the variation is between $1 - 3nm$ dependent on which cavity is measured. These values compare well to the prediction expected from the variation of the thickness of the initial oxide.

2.1.10 Anodic bonding

The discovery of the anodic bonding process by Pomerantz[14] has introduced an important method for hermetically sealing microelectronic, optical and MEMS devices. In this process the two wafers to be bonded are subjected to elevated temperature of up to $450°C$, DC voltage of up to $1000V$ and variable mechanical pressure.

In the case of anodic bonding of silicon and glass wafers the glass is at a negative potential with respect to the silicon (figure 2.12). The temperature increases the mobility if the sodium ions in the glass and they are attracted towards the cathode leaving region depleted of sodium ions at the anode (figure 2.11). If the anode happens to be the silicon wafer then the oxygen ions in the polarized part of the glass bind chemically with the silicon and form SiO_2.

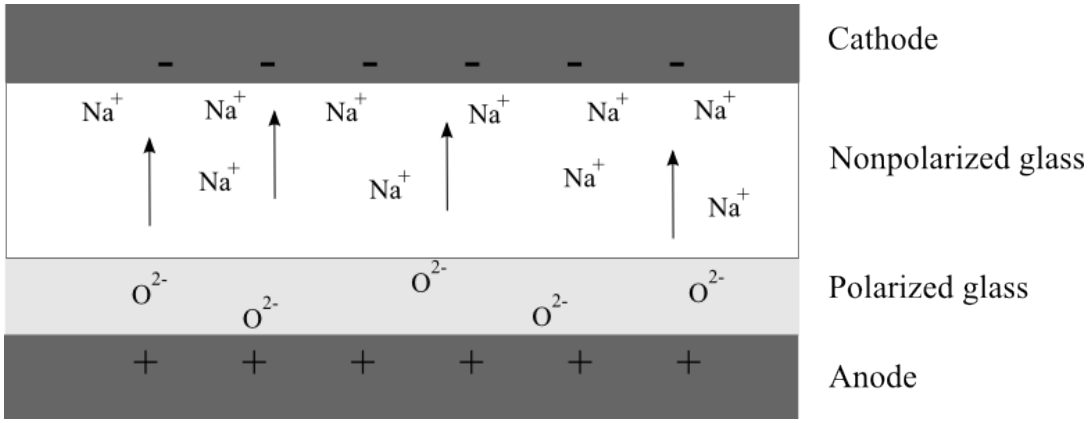

Figure 2.11: Anodic bonding process. The migration of sodium ions in the glass creates a polarized region near the silicon wafer, chemically bonding the glass and silicon.

The transformation of crystalline silicon to SiO_2 creates a bonding interface that is very strong. When attempts are made to separate the glass and silicon wafers by force sometimes the glass fractures rather than simply delaminating

from the silicon.

Cavity collapse

During the bonding process the surfaces of the cavity experience tensile stress due to the electric field. When the electric field is sufficiently high the surfaces are strained to a level that brings them into contact and they bond together. This irreversibly destroys the cavity gap.

A model for the collapse of microchannels during anodic bonding has been developed by Shih et. al.[13]. According to this model contact of the silicon and glass occurs over the cavity region if the following inequality holds:

$$V > \sqrt{\frac{E_{eff} d^3}{a \epsilon_a}} \tag{2.5}$$

where V is the voltage applied, $E_{eff} = 51.4GPa$ is the effective Young's modulus of the glass-silicon system, d is the depth of the cavity, a is *half* the width of the cavity and ϵ_a is the permittivity of air.

Given this we expected not to see collapse of the cavities if the voltage is kept bellow $850V$ for a cavity with width of $10mm$. However our observations showed that cavities larger than $3mm$ collapse even for the lowest feasible voltage $V_{min} = 400V$ for which bonding of the wafers occurs. Below V_{min} the wafers do not bond at all.

To resolve the problem of collapse we designed electrodes that have openings over the cavity region so that no electric field is present at that region. A test electrode is shown in figure 2.13.

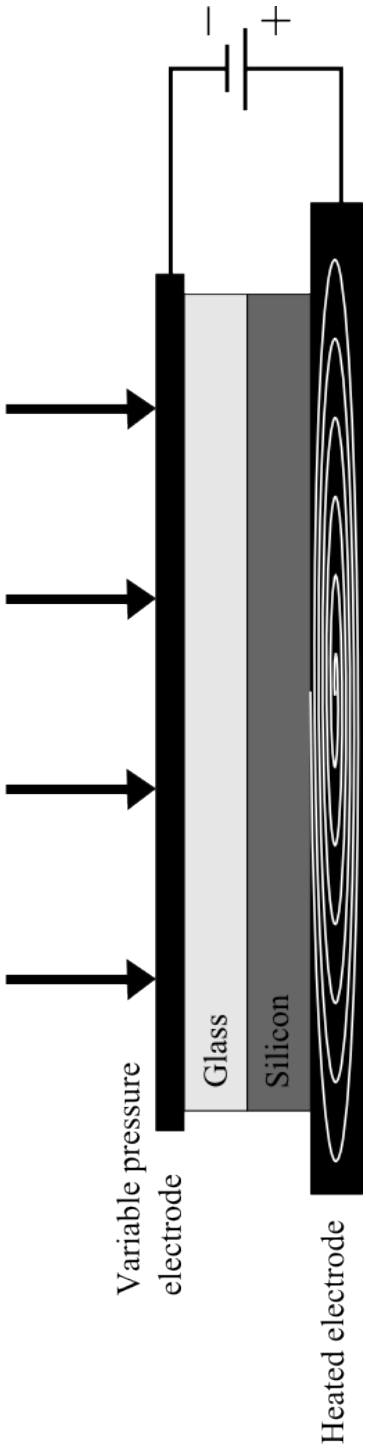

Figure 2.12: Anodic bonder.

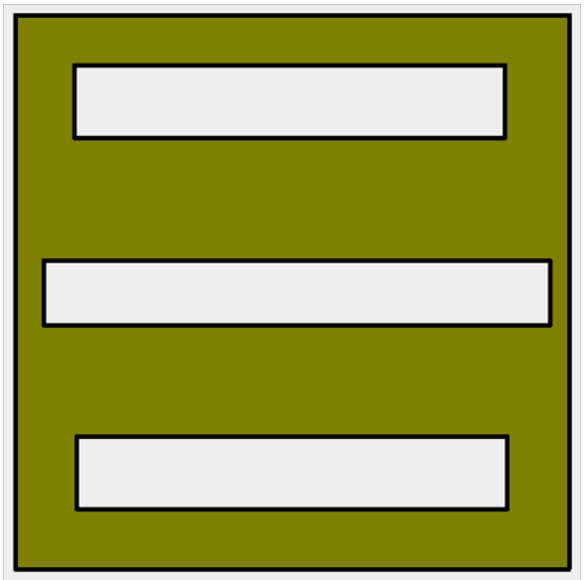

Figure 2.13: Test electrode used to exclude the electric field over some of the rectangular cavities.

The test electrode has been used to anodically bond a wafer patterned with rectangular cavities. As the conditions for that particular run are the same we see the effects of excluding the electric field from some of the cavities. Figure 2.14 shows that the devices with electric field in the cavity have completely collapsed while those without field over them have not. There is some bonding of the uncovered cavities at the edges because the electrode had cutout heights precisely the dimension of the cavities and some electric field had penetrated the patterned region.

Circular cell bonding procedure

To improve the uniformity of the cavity depth during the thermal cycling we have used a specialty borosilicate glass from Hoya Corp. The SD-2 glass is matched to have coefficient of thermal expansion similar to silicon (figure 2.15).

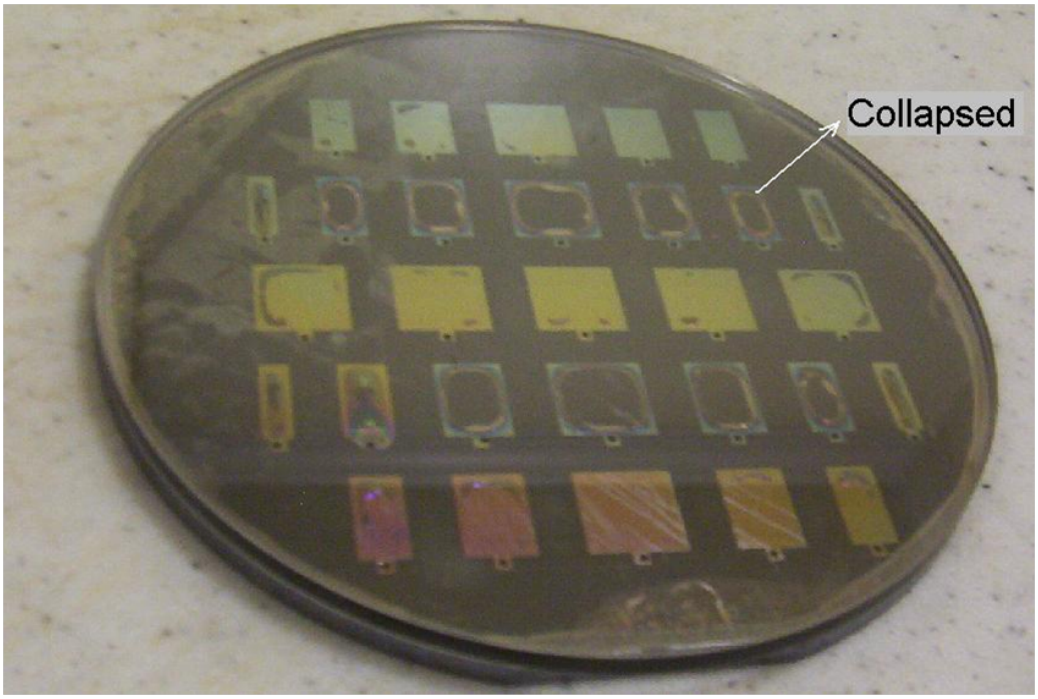

Figure 2.14: Testing the effect of excluding the electric field over some of the cavities. All cavities that had an electrode over them have collapsed.

When the pieces for the cell are cleaned we put them on the bottom electrode of the *EV 501* anodic bonder, silicon being first with the cavity pattern facing up, followed by the glass. Around the pieces for the cell we put scrap pieces of bonded silicon-glass to complement the stack to a full wafer. The extra pieces are needed to ensure that the top electrode does not tilt when force is applied to it. An electrode with circular hole with diameter $D = 11mm$ is put on top of the glass. The hole is aligned to be concentric with the cavity.

The lid of the anodic bonder chamber is closed and force of $70N$ is applied to the top electrode by an automatic piston over the whole area of the wafer ($\approx 75cm^2$). The piston contains an electrical lead that comes into contact with the top electrode. The wafer assembly is heated to $350°C$. Once the temperature

equilibrates, a voltage of $450V$ is applied in between the electrodes for 8 minutes. We observe current of $10mA$ flowing through the silicon-glass stack. After the voltage is removed the stack is gradually cooled to room temperature and the bonded pieces taken out of the chamber.

Cavity depth

After the anodic bonding was complete, the depth of the cavity was measured through interferometry. The results showed that the depth of the cavity is $640\,nm$. We have used this value for the calculations of our measurements.

2.1.11 Final preparation of the cell

After the anodic bonding is finished we are left with a cell for which the glass is not symmetric with respect to the axis of the cavity. To resolve this issue we need to trim the excess glass so that it has exactly the same dimensions as the silicon piece. To prevent contamination of the cell through the fill line hole during the dicing the silicon side of the cell is covered with several layers of packing tape. Afterwards the cell is glued to the magnetic holder with the glass side down using the bonding polymer. The cell is not completely surrounded by the polymer as in the first dicing procedure, but has only a thin layer between the holder and the glass.

To trim each side of the glass we first align the saw blade while stopped to be parallel to the silicon by touching the vertical wall of the silicon piece (figure 2.16). After that the blade is spun and the glass cut. These steps are repeated for

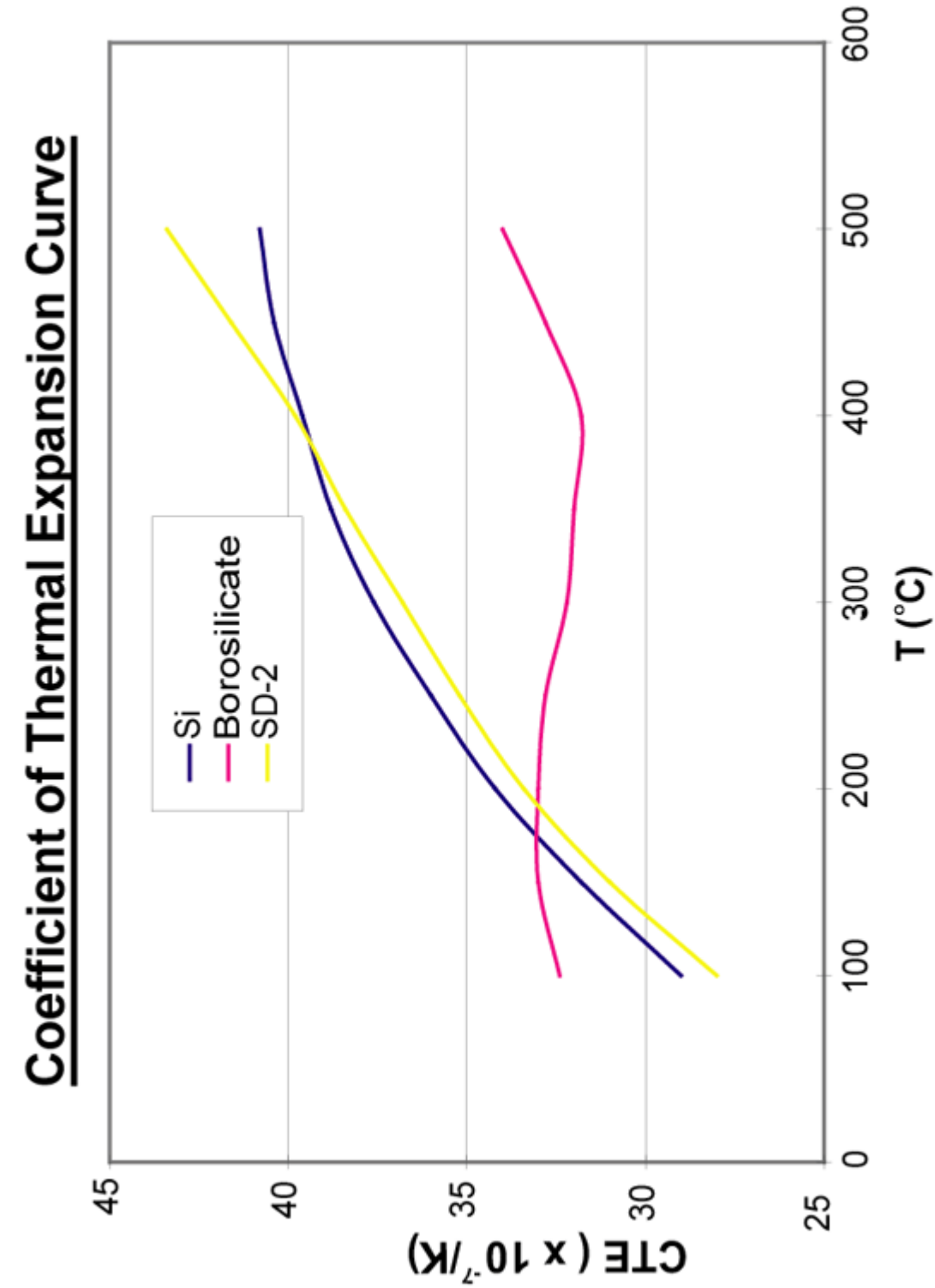

Figure 2.15: Thermal expansion of different materials used during the anodic bonding.

e

the remaining sides of the cell. When all sides trimmed the cell is removed from the holder and the remaining bonding polymer is cleaned with cotton swabs dipped in acetone.

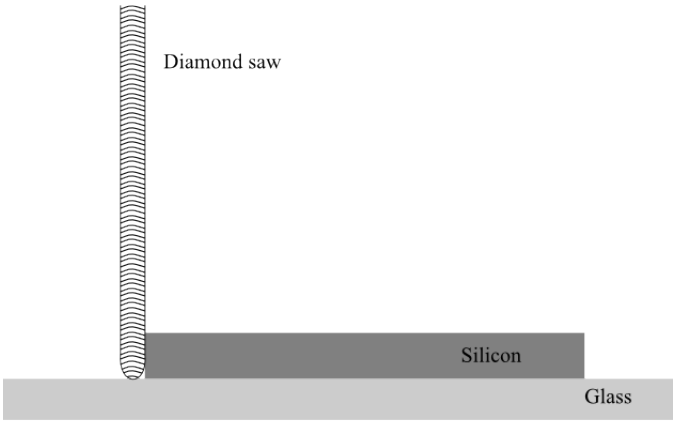

Figure 2.16: Trimming the excess glass.

2.2 Making the mechanical parts and assembling the torsional oscillator

The mechanical parts for the torsional oscillator were made with common machining techniques. Due to the small dimensions of the torsion rod it was machined in the professional shop. The rest of the parts were made in the student workshop.

2.2.1 Making the parts

The torsional rod

The torsional rod for the oscillator has been made of coin silver consisting of 90% silver and 10% copper. The dimensions of the rod are given in figure 2.17.

One of the challenging steps in the machining is the drilling of the fill line through the whole body. The majority of the fill line is drilled with a long index drill number 69. To finish the fill line an electrical discharge machine (EDM) is used. During the EDM process a rapid electrical arc is induced between the workpiece and the electrode. The arcing evaporates the material and the electrode is advanced to drill deeper. The wire electrode with diameter 0.008″ is inserted through the long drilled hole and carefully aligned not to touch the walls of the fill line.

After the torsional rod is machined it is sonicated for 20 minutes in isopropanol to remove all oil contaminants. After the alcohol evaporates the rod is annealed in a furnace at $650°C$ for 2 hours.

The wings

The electrodes (wings) for the drive and detection are made out of magnesium to reduce their moment of inertia when mounted on the torsional rod. Their dimensions are tailored to match the slots in the rod with a little flop allowed for the epoxy needed to attach them. The height of each wing is 0.375″, the width is 0.800″ and the thickness is 0.120″.

After machining, the wings are carefully polished on a mechanically flat plate using 1200 grit sandpaper.

The clamps and electrodes

The torsional oscillator is mounted on the heat exchanger of the cryostat using copper clamps. The electrodes used to drive the oscillator and detect the signal are attached to the base plate. The assembly is shown in figure 2.20.

2.2.2 Assembling the oscillator

Putting the wings

The magnesium wings are attached to the torsional rod using Stycast 1266 epoxy. If the epoxy is applied directly over the metal parts it tends to slide off the polished surfaces during the curing and the joint may end having air pockets.

To ensure that the Stycast is distributed evenly at the joint we soak a piece of Kodak lens cleaning paper in the epoxy and press it into the slots in the body of the torsional rod with the magnesium wing. After the epoxy has cured the excess paper that sticks out of the rod-wings joint is carefully trimmed with a razor blade.

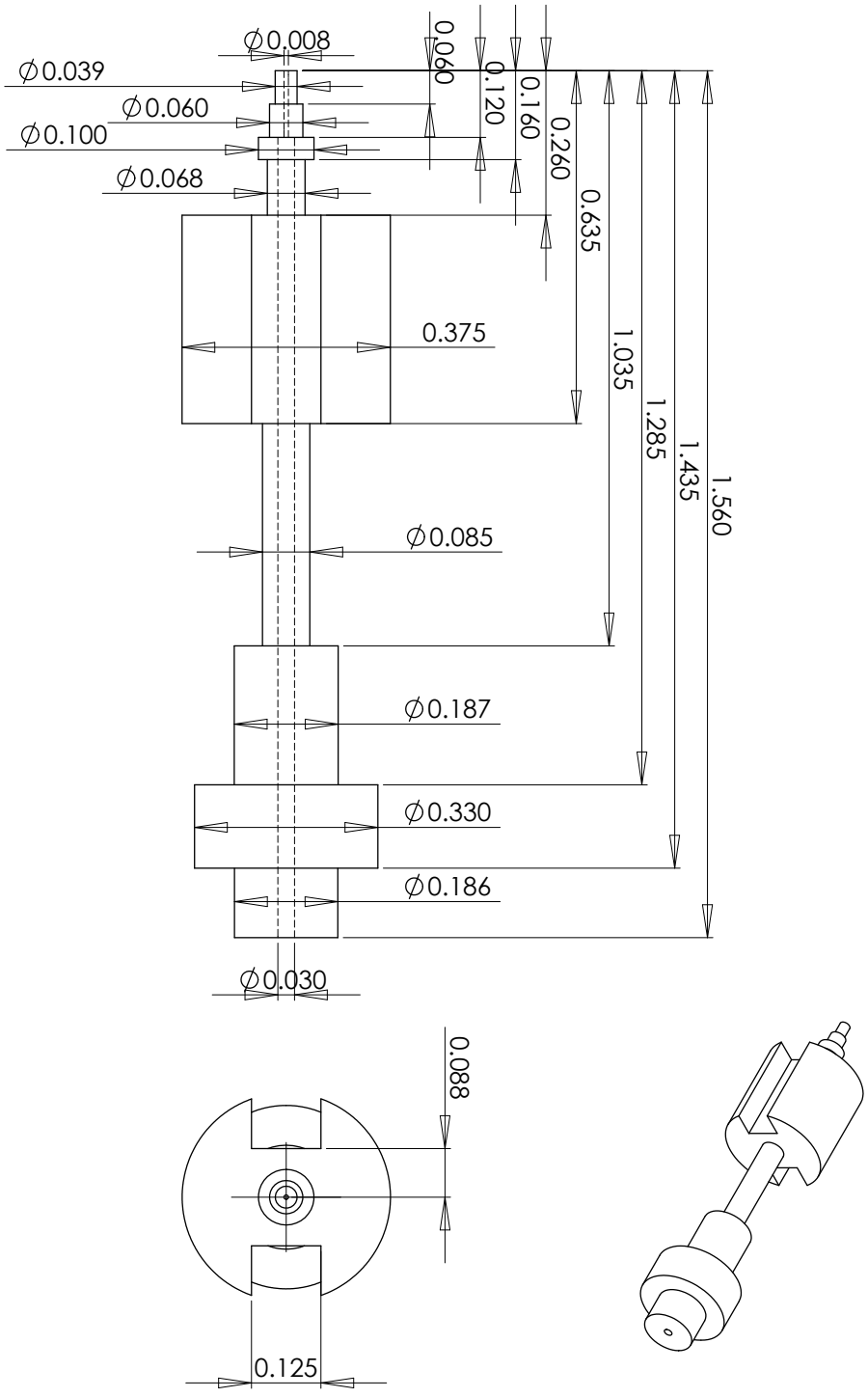

Figure 2.17: Torsional rod. All units are in inches.

Mounting the head

To mount the head of the oscillator to the torsional rod a small amount of Stycast 2850 epoxy is placed on the rod as shown in figure 2.18. With slow twisting motion the rod is placed in the drilled fill line of the cell. When the rod is in place the cell is rotated several times around it to ensure even distribution of the epoxy. The step in the silicon prevents the Stycast from entering into the cavity.

Since the Stycast needs to stay overnight to cure we need to ensure that the head remains perpendicular to the rod during that time. A jig to support the oscillator was made in advance (figure 2.19). The dimensions of the jig are such that when the rod is supported by its wings the head remains flush with the rod and the jig. The jig is kept upright with the oscillator head on top to prevent epoxy from slowly flowing into the cavity while still viscous.

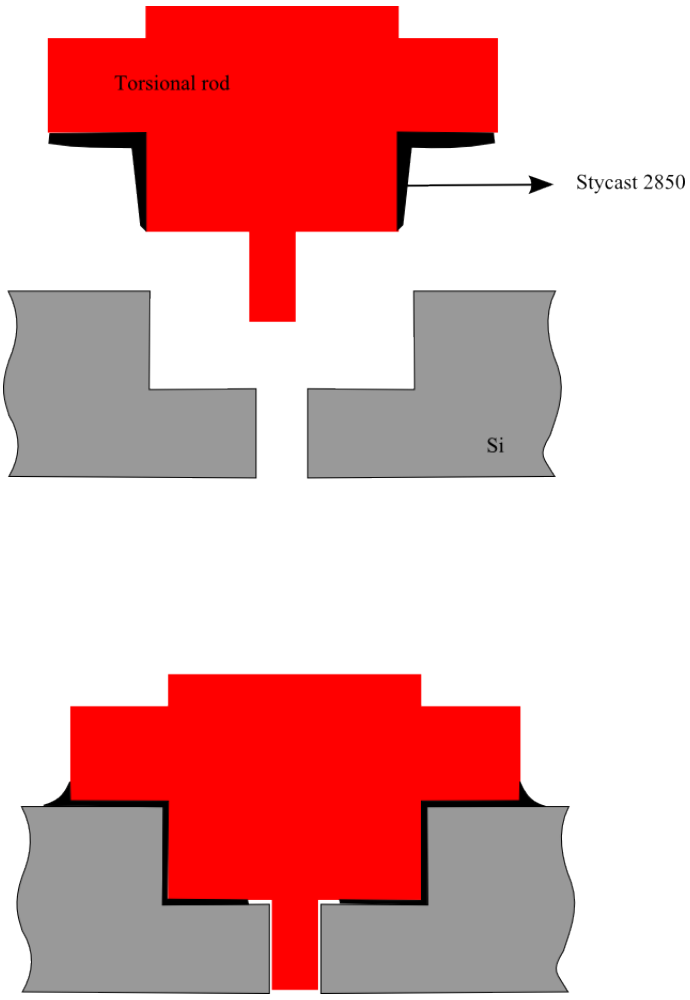

Figure 2.18: Distribution of the epoxy during the mounting of the cell.

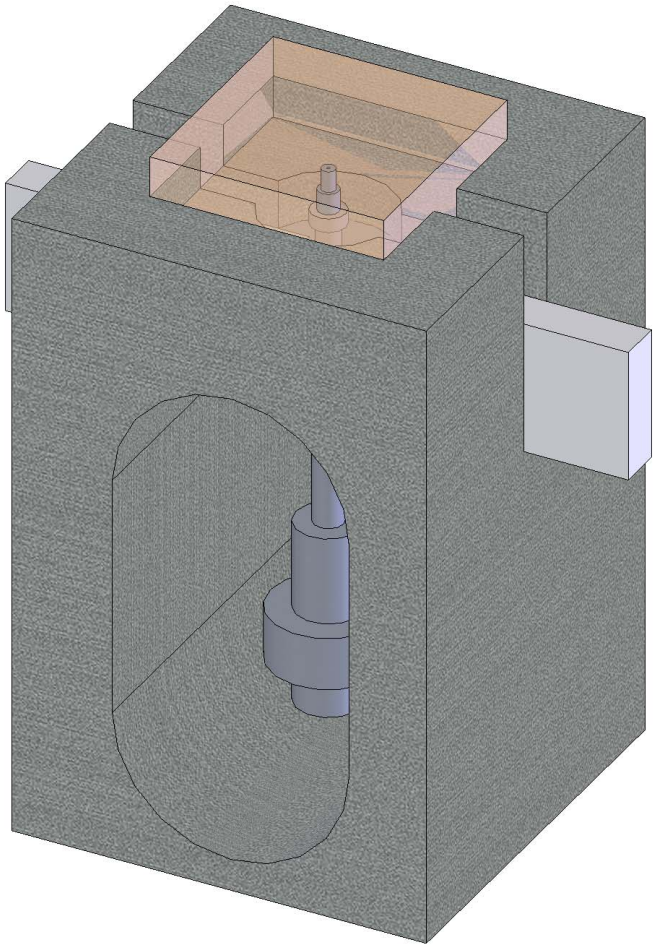

Figure 2.19: Jig for leveling the head of the oscillator with the torsional rod.

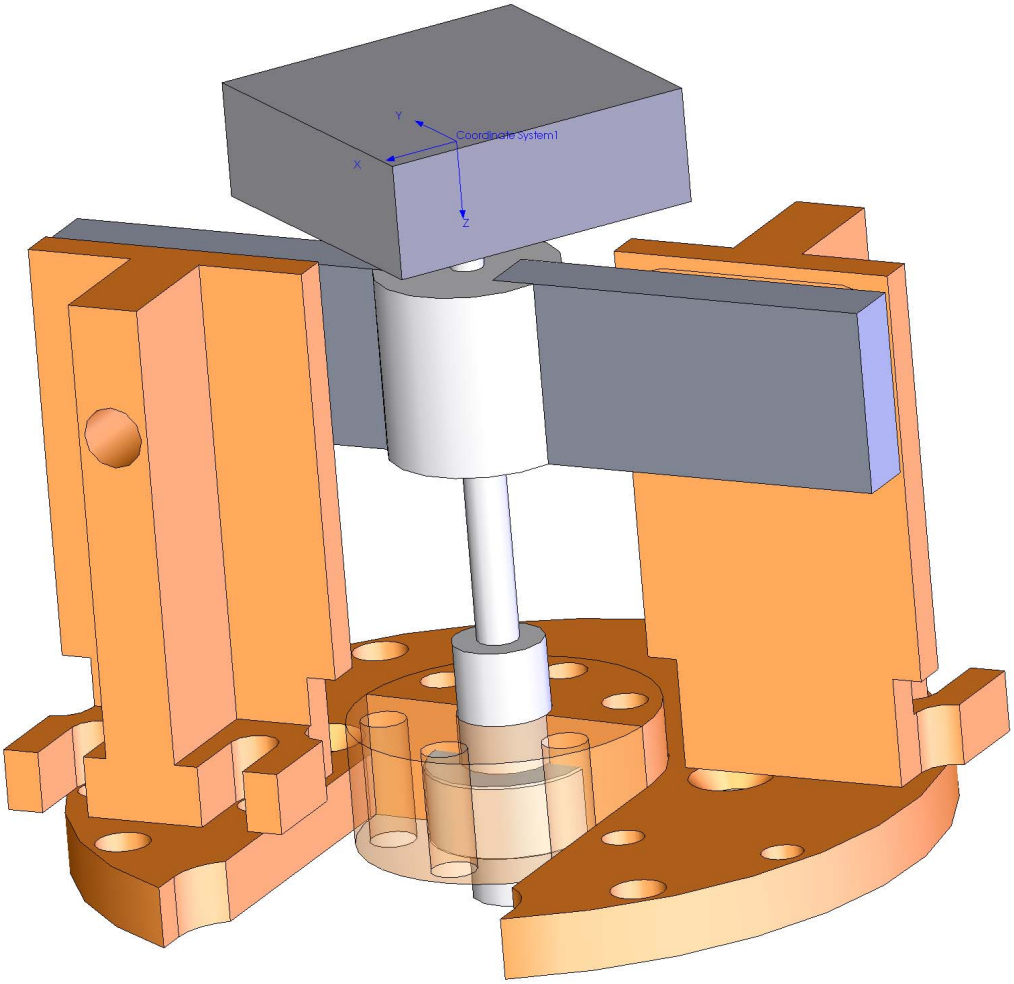

Figure 2.20: Torsional oscillator before it is attached to the heat exchanger.

2.2.3 Completing the oscillator

After the Stycast cures and the head of the oscillator is secured to the the torsional rod we deposit $3\mu m$ of silver to increase the thermal conductivity between the head and the silver rod. The whole head and the joint with the rod are covered. The silver is deposited through sputtering which keeps the temperature of the oscillator low during the deposition and the epoxy joints are not affected by thermal damage.

The epoxy joining the wings to the body of the oscillator keeps them electrically isolated from the rest of the oscillator. In order to drive the oscillator and detect the response signal the wings must be grounded by coupling them to the cryostat via the torsional rod. To do so a fine copper wire is attached to each wing and the torsional rod through silver paint. The resistance between the wings and the rod is measured with an ohm meter to be less than 5Ω.

CHAPTER 3

SURFACE ANALYSIS

The characteristics of the surfaces of the cell are important for the behavior of the shear flow. In our experiment we observed complete decoupling of the normal ^3He fluid from the oscillator over much of the temperature range. This decoupling prevented the study of the superfluid properties of the helium.

To better understand the decoupling we compared the surface topography of our cell with the highly polished surfaces used for a related experiment by Casey et al.[10]. In their case the decoupling is still observed but is not complete.

3.1 Surface height distribution function and RMS

An important characteristic of the surface profile is the one dimensional height distribution function $p(h)$. It gives the probability of particular height h occurring at some point on the surface. This function is normalized in the following manner:

$$\sum_h p(h) = 1 \tag{3.1}$$

It is preferable that the height distribution function be determined directly from the profile being studied. However, if mathematical simplicity is required for description of the distribution, the central limit theorem of the sum of large number of random variables dictates that a Gaussian distribution is a good approximation, with the root mean square being the variance:

$$p(h) = \frac{1}{\sqrt{2\pi}W_{rms}} exp\left(-\frac{h^2}{2W_{rms}^2}\right) \tag{3.2}$$

The root mean square roughness is a simple measure of the profile height roughness that characterizes the fluctuations of the surface height around the average surface height and is defined as:

$$W_{rms} = \sqrt{\frac{1}{n}\sum_{i=1}^{n}\left(h(x_i) - \bar{h}\right)^2} \tag{3.3}$$

with n points and $h(x_i)$ being the height at point x_i, and the average height of the profile given as:

$$\bar{h} = \frac{1}{n}\sum_{i=1}^{n} h(x_i) \tag{3.4}$$

3.2 Autocorrelation

While the height distribution function gives information about the first order statistics of an independent point at position (x, y), it does not reflect the correlations between points at different positions. Because of that, it is possible to have different surface profiles with the same RMS and height distribution function. To account for this, the two dimensional spatial autocorrelation function is introduced. For a random function of the position $F(x, y)$ it is defined as:

$$C(x_1, y_1) = \int_{-\infty}^{\infty}\int_{-\infty}^{\infty} F^*(x, y)F(x + x_1, y + y_1)dxdy \tag{3.5}$$

It is possible to evaluate $C(x, y)$ directly from equation 3.5, but it is very inefficient in terms of computational time. To improve the speed of computation the Fourier transform of $F(x, y)$ is introduced:

$$f(k_x, k_y) = \int_{-\infty}^{\infty} \int_{-\infty}^{\infty} F(x, y) e^{-(xk_x + yk_y)} dxdy \tag{3.6}$$

And the inverse transform is given by:

$$F(k_x, k_y) = \frac{1}{4\pi^2} \int_{-\infty}^{\infty} \int_{-\infty}^{\infty} f(k_x, k_y) e^{+(xk_x + yk_y)} dk_x dk_y \tag{3.7}$$

Thus the two dimensional spatial autocorrelation function can be written as:

$$\begin{aligned} C(x_1, y_1) = \int_{-\infty}^{\infty} \int_{-\infty}^{\infty} dxdy \frac{1}{4\pi^2} \int_{-\infty}^{\infty} \int_{-\infty}^{\infty} dk'_x dk'_y f^*(k'_x, k'_y) e^{-i(x_1 k'_x + y_1 k'_y)} \\ \frac{1}{4\pi^2} \int_{-\infty}^{\infty} \int_{-\infty}^{\infty} dk''_x dk''_y f(k''_x, k''_y) e^{\left((x_1 + x)k''_x + (y_1 + y)k''_y\right)} = \\ = \frac{1}{(4\pi^2)^2} \int_{-\infty}^{\infty} \int_{-\infty}^{\infty} dxdy \int_{-\infty}^{\infty} \int_{-\infty}^{\infty} dk'_x dk'_y \\ \int_{-\infty}^{\infty} \int_{-\infty}^{\infty} dk''_x dk''_y f^*(k'_x, k'_y) f(k''_x, k''_y) e^{i\left((k''_x - k'_x)x + (k''_y - k'_y)y\right)} e^{i(k''_x x_1 + k''_y y_1)} \end{aligned} \tag{3.8}$$

Considering that:

$$\int_{-\infty}^{\infty} \int_{-\infty}^{\infty} dxdy \, e^{i\left((k''_x - k'_x)x + (k''_y - k'_y)y\right)} = 4\pi^2 \, \delta(k''_x - k'_x) \, \delta(k''_y - k'_y) \tag{3.9}$$

The autocorrelation function becomes:

$$C(x_1, y_1) = \frac{1}{4\pi^2} \int_{-\infty}^{\infty} \int_{-\infty}^{\infty} dk'_x dk'_y \, f^*(k'_x, k'_y) f(k''_x, k''_y) \delta(k''_x - k'_x) \delta(k''_y - k'_y) = \\ = \frac{1}{4\pi^2} \int_{-\infty}^{\infty} \int_{-\infty}^{\infty} \left| f(k_x, k_y) \right|^2 e^{i(x_1 k_x + y_1 k_y) dk_x dk_y} \tag{3.10}$$

Thus the autocorrelation function of the random variable $F(x, y)$ can be obtained by the inverse Fourier transform of the square modulus of the Fourier transform of $F(x, y)$.

Apart from the increase of computational speed, the use of the Fourier transform introduces an easy way to filter out unwanted frequencies from the raw data of the surface profile. Since it is common for the AFM to introduce low frequency noise to the output data the filtering will be very useful to us. There are many algorithms for finding the Fourier transform of a function but without arguing the most popular is the Fast Fourier Transform. The only requirement for the FFT is that the number of columns and rows of the data be a power of 2. Since our data is always 512x512 points it can be readily used.

3.3 Sample preparation and measurements

The topographies of the silver sample and the polished Borofloat glass used for the current experiment are obtained from the unmodified samples as received from the manufacturers.

The roughness of the thermal oxide grown on the wafers is measured over the patterned regions after the oxidation of chapter 2.1.4.

The roughness of the silicon wafers used for the torsional oscillator cell is

measured after the thermal oxide is removed from the surface as in section 2.1.9. It should be noted that all silicon wafers exposed to air will grow 12 – 19Å thick native oxide at room temperature, thus the measurements are not done directly on the silicon crystal but rather on the native oxide.

A silicon wafer that was dry etched using the Bosch process has also been characterized. The wafer did not have any initial oxide.

Roughened glass pieces were prepared by immersing polished glass in a dilute BOE (30:1) for various lengths of time.

Prior to the data acquisition the samples are immersed for 30 minutes in acetone and immediately before scanning are swabbed with an isopropanol soaked q-tip.

To obtain the topography of particular sample, it is loaded in the *DI 3100* atomic force microscope and a ”tapping” cantilever is installed in the scanning head. The tip of the cantilever used for probing has a diameter of 10Å. The scanning head is brought into contact with the sample and the gain parameters and scan speed are chosen such that the head follows the surface profile closely. The highest resolution for the microscope, which is 512x512 pixels, is chosen for all scans. The size of the area scanned under the probe is selected between $2\mu m \times 2\mu m$ and $50\mu m \times 50\mu m$.

3.4 Data analysis and results

The results for the surface characterization of the coin silver, the roughened and polished glass, the oxidized/bare silicon wafers are reported in this section.

Detailed explanation for the analysis of the silver surface along with the most important analysis for the glass surfaces is given along with the results for the remaining materials.

The raw data for the topography of the $10\mu m \times 10\mu m$ silver scan is given in figure 3.1 and the surface of the polished glass is given on figure 3.2. For random surfaces one would expect the autocorrelation function to be independent of the orientation of the coordinate system. The autocorrelation function of the raw data for the polished silver is given on figure 3.3.

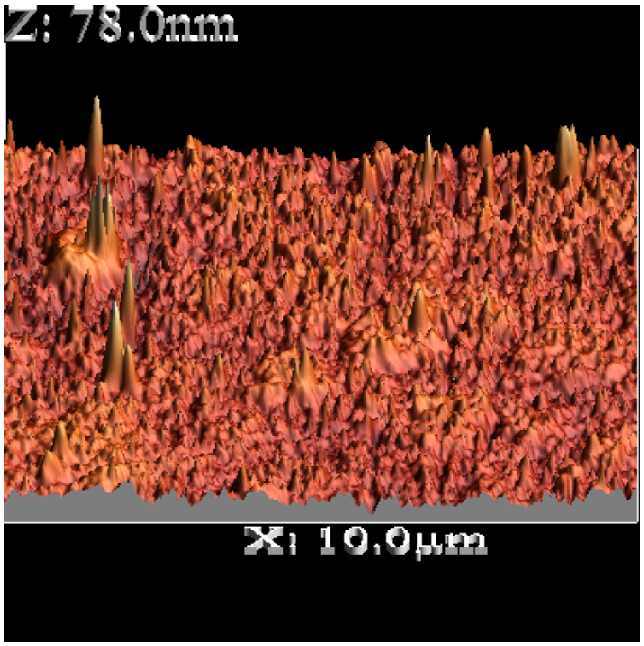

Figure 3.1: Surface profile of polished coin silver. Both X and Y axes are $10\mu m$ long. The maximum height of the surface is $78nm$.

Careful observation reveals that the correlation peak is surrounded by long wavelength variation independent of the orientation of the coordinate system. This variation does not change direction if the wafer is rotated during a particular scanning session. The presence of the long wavelength variations is at-

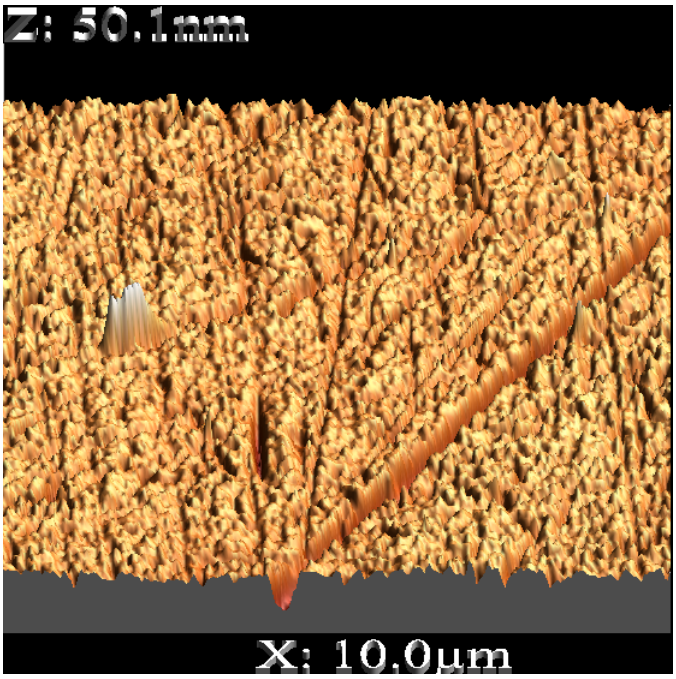

Figure 3.2: Surface profile of polished glass.Both X and Y axes are $10\mu m$ long. The maximum height of the surface is $50nm$.

tributed to a feedback in the electronics of the microscope.

The long wave pattern inevitably increases the width of the autocorrelation and thus will give a higher value for the correlation length than it actually is. In order to study the long wavelength contribution a low-pass filter is created as follows: The Fourier transform of the raw data is taken and wavelengths shorter than $1/k = 1\mu m$ are discarded (figure 3.4a). The cutoff is selected such that it is longer than the width of the central peak and at the same time shorter than the expected length (visually determined to be $\approx 1/4$ of the scan length) of the of the long wavelength fluctuations. The modulus of resulting k-space is taken and then it is squared (figure 3.4b) followed by the inverse Fourier transform (figure 3.5) resulting in autocorrelation function dominated by the long wavelengths.

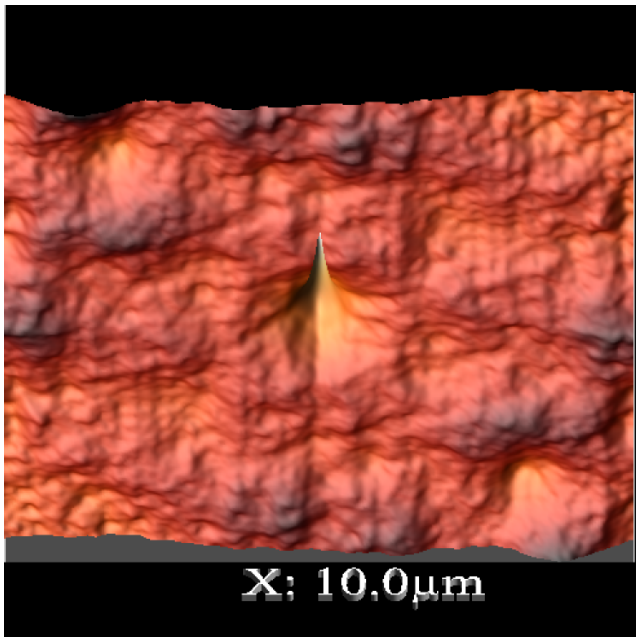

Figure 3.3: Autocorrelation function for the $10 \times 10 \mu m$ silver scan before filtering.

A cross-section through the maximum of the autocorrelation has been taken in direction of the steepest descent insuring that it is perpendicular to the ”valleys”. The distances between the maxima or minima are measured and the dominating long wavelength is determined. Depending on which point is taken for a reference the wavelength is determined to be between $2.8 \mu m$ and $3.1 \mu m$ (figure 3.6.

Knowing the long wavelengths that would affect the measurement of the correlation length of the sample, a high pass filter is created to eliminate the unwanted frequencies. The procedure is the same as for the low pass filter with the only distinction that the long waves are discarded.

The k-space discarded should be as small as possible in order to give better presentation of the correlation length (still big enough to eliminate the un-

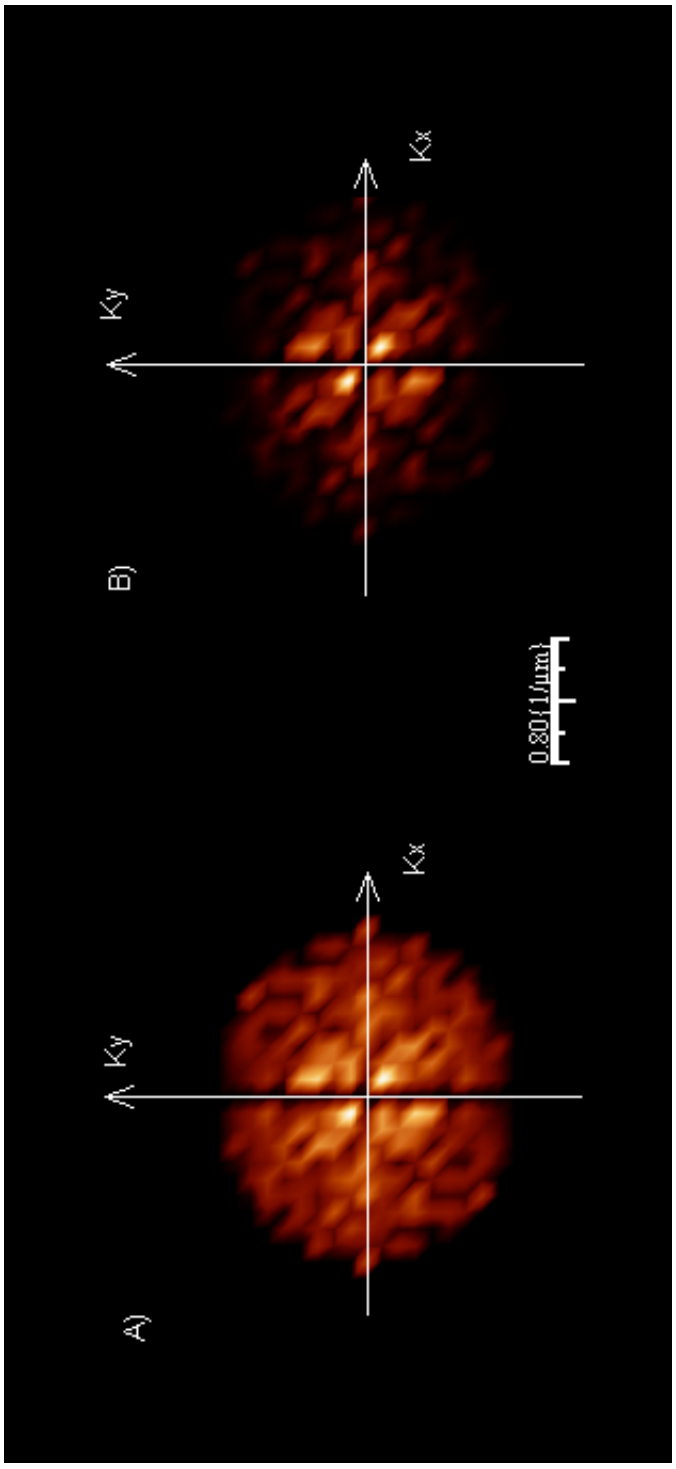

Figure 3.4: A): The k-space used for the low-pass filter is such that $\sqrt{k_x^2 + k_y^2} \leq (1\mu m)^{-1}$. B): The modulus squared of a). The brightness of both figures is not to the same scale.

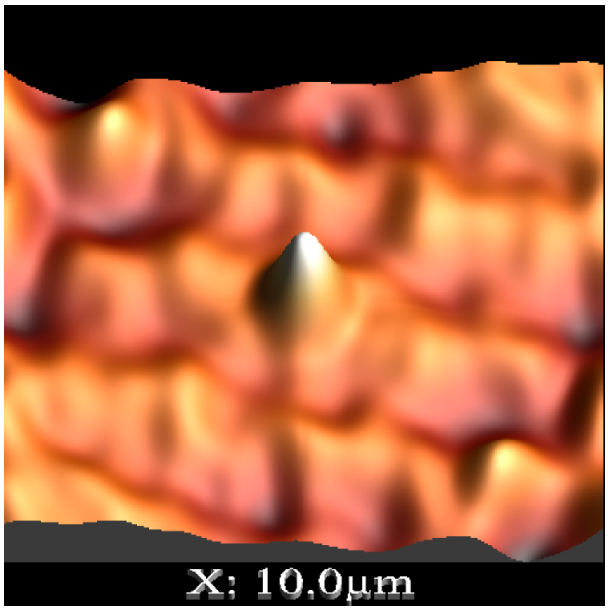

Figure 3.5: Autocorrelation of the surface after the low pass filter is applied. The dominating wavelength is measured from the distances between the peaks.

wanted frequencies. The k-space is chosen to be $\sqrt{k_x^2 + k_y^2} \geq (2.5\mu m)^{-1}$. Following the same procedure as above, the autocorrelation function is calculated and plotted on figure 3.7.

It is evident that the high pass filter substantially reduces the unwanted variations, despite that the cutoff wavelength is very close to the dominant one as obtained in the low pass analysis.

In order to calculate the correlation length, a cross-section through the peak is taken (figure 3.8). The cross-section of the correlation peak for the polished glass is given in figure 3.9. The profiles of the cross-sections are then fitted to a Lorentzian.

Since the profile is fitted very well to a Lorentzian, it is natural to define the

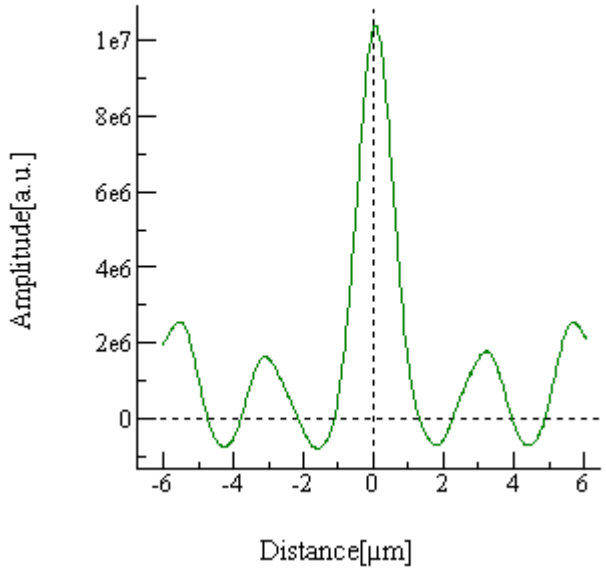

Figure 3.6: The long wavelength introduced by the AFM for the silver surface is measured to be between 2.8μm and 3.1μm

correlation length as *half* the width of the Lorentzian. The reason for using only half of the width is that the correlation length is the maximum displacement distance at which significant correlation occurs and the autocorrelation function is symmetric with respect to the origin.

The fitting parameters for the Lorentzian yield width $\Gamma = 238nm$, thus the correlation length equals to $L_c = 119nm$.

So far the correlation length of the $10 \times 10\mu m$ silver scan has been determined which gives the lateral characteristics of the surface topography. In order to completely describe the surface, the root mean square of the surface height is calculated.

The height distribution of the surface topography of silver ($RMS = 4.09nm$)

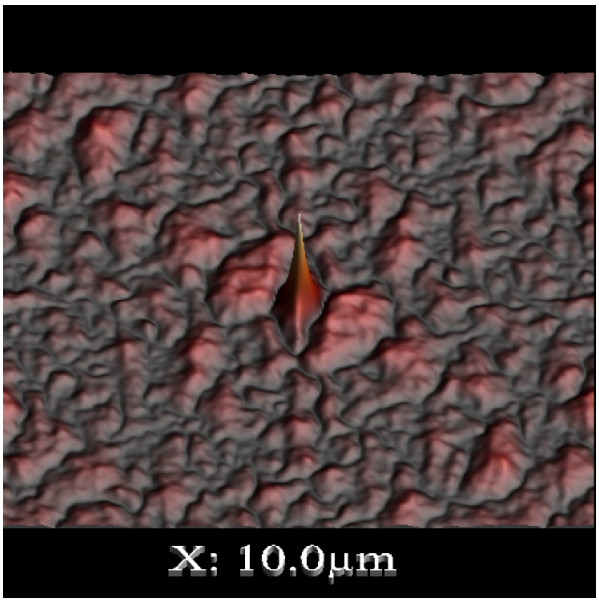

Figure 3.7: Autocorrelation function of the silver surface after the high pass filter is applied (the long wavelengths are discarded).

is given in figure 3.10 together with the Gaussian fit with width equal to the RMS. Similarly the height distribution of the polished glass ($RMS = 2.49nm$) is given in figure 3.11

We observe that the simple measure of the RMS gives good approximation to the height distribution of the profile especially for heights above the mean.

Up to this point techniques for obtaining the correlation length and the root mean square of the surface height have been developed. Using the same procedures the surfaces of the thermal oxide on silicon, polished and etched glass and silicon wafers have been characterized for different scan dimensions.

The results are summarized in table 3.1.

Table 3.1: Roughness parameters for different materials.

Material (scan size)	R=Correlation length	Height RMS	l=Average height	R/l
Coin silver ($5x5\mu m$)	$112nm$	$4.38nm$	$13.7nm$	8.15
Coin silver ($10x10\mu m$)	$119nm$	$4.09nm$	$12.8nm$	9.27
Coin silver ($50x50\mu m$)	$110nm$	$5.40nm$	14.1	7.80
Polished glass ($10x10\mu m$)	$69nm$	$2.49nm$	$24.7nm$	2.79
Silicon wafer (after thermal oxidation) ($10x10\mu m$)	$17^{*}nm$	$0.26nm$	$3.5nm$	4.86
Silicon wafer (after thermal oxidation) ($2x2\mu m$)	$2^{*}nm$	$0.24nm$	$2.7nm$	0.74
Thermal oxide on silicon ($10x10\mu m$)	$18^{*}nm$	$0.53nm$	$2.4nm$	7.5
Glass etched 5 minutes in 30:1 BOE ($10x10\mu m$)	$92nm$	$3.63nm$	$36nm$	2.56
Glass etched 15 minutes in 30:1 BOE ($10x10\mu m$)	$110nm$	$3.76nm$	$38nm$	2.89
Silicon wafer after reactive ion etch ($5x5\mu m$)	$14^{*}nm$	$0.31nm$	$1.7nm$	8.24

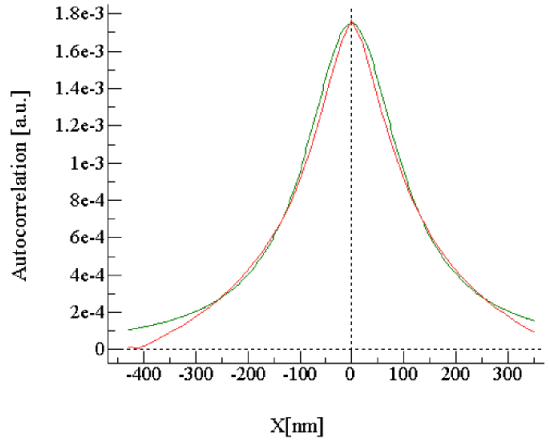

Figure 3.8: Cross section of the autocorrelation function after the high-pass filter has been applied. The red line is the data and the green line is the Lorentzian fit for the polished silver.

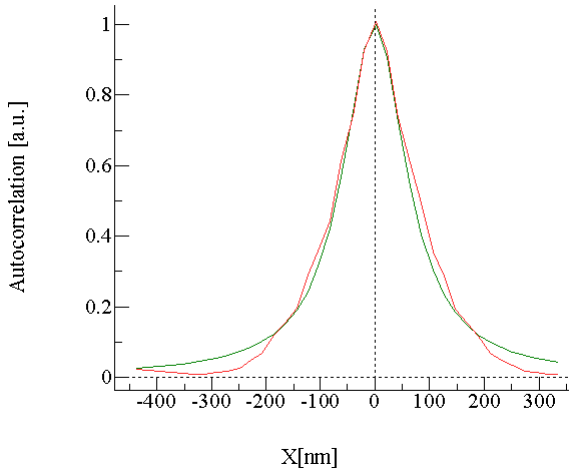

Figure 3.9: Autocorrelation function for the polished glass after the high-pass filter has been applied. The red line is the data and the green line is the Lorentzian fit.

3.5 Discussion

The polished surfaces of different materials have been characterized for various scan sizes. We measure that the correlation length of the silver sample is the

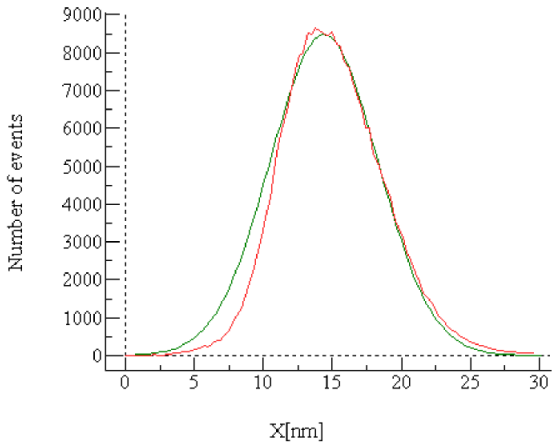

Figure 3.10: Height distribution for the polished silver (red line) and the Gaussian fit (green line) to it with width equal to the $RMS = 4.09nm$ for polished silver. The average height is $12.8nm$.

same (up to 10% error) regardless on the scan size. While the RMS for the $50 \times 50\mu m$ region is somewhat higher than the other two regions it is attributed to several very high peaks on the topography (possibly dirt) and a rather deep scratch that are not present on the smaller areas.

An important note is due for the correlation lengths of the silicon wafers (both bare and oxidized). The surface scanned is so smooth that the limit of the lateral resolution for the AFM is reached. The correlation function is delta-like function and the Lorentzian fit is not considered reliable since there are only 3 points to fit it through. Because of that the data quoted above should not be taken to be the real correlation length especially considering the strong dependence on the scan size. This comes as no surprise as the single crystal silicon wafers are manufactured to have atomically flat surfaces. The conclusion therefore that can be drawn is that the correlation length is less than the quoted values.

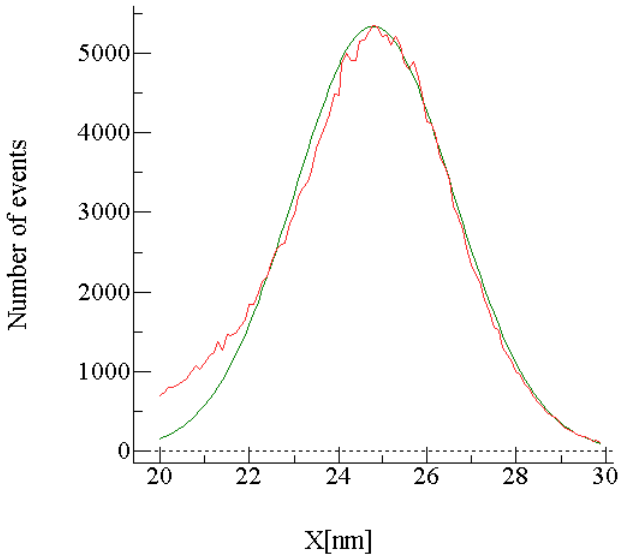

Figure 3.11: Height distribution (red line) and the Gaussian fit (green line) to it with width equal to the $RMS = 2.49nm$ for polished glass. The average height is $24.7nm$.

The Bosch etched silicon has higher RMS than that of the silicon of the thermally oxidized wafer. Still it is too smooth to get the correct value for the correlation length. Thus to obtain higher roughness for the silicon a different method for manufacturing has to be employed.

The polished glass that we have used for the construction of the cell of the torsional oscillator has been determined to be smoother than the silver surfaces but considerable rougher than the opposing silicon surface of the cell. We have been able to increase the roughness of the glass to parameters similar to that of the polished silver by immersing it in diluted HF. By varying the time in the bath and the concentration of the acid the glass roughness can be tailored to the desired parameters.

CHAPTER 4

THE EXPERIMENT

This chapter reports the behavior of the normal fluid of ^3He in our torsional oscillator. We tried to determine the level to which it is coupled to the cavity in the head. Our measurements showed partial coupling of the normal fluid to the oscillator at $160\,mK$ which decoupled further as the temperature was lowered, becoming fully decoupled below $100\,mK$.

4.1 Torsional oscillator equations

We will first describe the oscillatory motion of an incompressible fluid bounded by two infinite planes yz in the y direction. Because of the symmetry of the torsional oscillator we require the planes to be at $x = \pm d/2$ where d is the thickness of the gap in which the fluid is constrained. The oscillatory motion happens with frequency ω. Landau and Lifshitz[15] treat this problem for an incompressible fluid without slip.

The velocity of the plane is of the form:

$$u = A\cos(\omega t) \tag{4.1}$$

For convenienve we write it as:

$$u = Re\left(u_0 e^{-i\omega t}\right) \tag{4.2}$$

To simplify the notation further we will drop the Re sign and we will take the real part of the final result.

As we are ignoring the slip for the moment, the boundary conditions require that the velocity of the fluid is equal to that of the walls for its boundary layer, i.e.:

$$v_y(-d/2) = v_y(d/2) = u_0 e^{-i\omega t} \tag{4.3a}$$

$$v_x = v_z = 0 \tag{4.3b}$$

From the symmetry we see that the velocity of the fluid layers will depend only on the time and the position x.

For a viscous incompressible fluid the Navier-Stokes equation is:

$$\frac{\partial v}{\partial t} + (\vec{v} \cdot \nabla)\,\vec{v} = -\frac{1}{\rho}\nabla P + \frac{\eta}{\rho}\nabla^2 \vec{v} \tag{4.4}$$

The equation of continuity is $\nabla \vec{v} = 0$. Since $v_x = 0$ from the boundary conditions and since all quantities are independent on y and z we have:

$$(\vec{v} \cdot \nabla)\,\vec{v} = 0 \tag{4.5}$$

From the symmetry we also see that the velocity is in the y direction. Thus the equation of motion simplifies to:

$$\frac{\partial v}{\partial t} = \left(\frac{\eta}{\rho}\right)\frac{\partial^2 v}{\partial x^2} \tag{4.6}$$

For this differential equation the solutions are of the form:

$$v = u_0 \frac{\cos(kx)}{\cos(kd/2)} e^{-i\omega t} \tag{4.7}$$

with

$$k = \pm(1+i)\sqrt{\frac{\rho\omega}{2\eta}} = \pm\frac{(1+i)}{\delta} \tag{4.8}$$

where δ is the viscous penetration depth:

$$\delta = \sqrt{\frac{2\eta}{\rho\omega}} \tag{4.9}$$

To find the frictional force on the surface we must calculate the σ_{xy} component of the stress tensor:

$$\sigma_{xy} = \eta \frac{\partial v_y}{x}\bigg|_{x=d/2} = u_0 \eta k \frac{\sin(kx)}{\cos(kx/2)} e^{-i\omega t}\bigg|_{x=d/2} = u_0 \eta \frac{1+i}{\delta} \tan(kd/2) e^{-i\omega t} \tag{4.10}$$

At this point we should note that for oscillations with small amplitudes as in our case, the term $(\vec{v} \cdot \nabla)\,\vec{v}$ in the Navier-Stokes equation is small compared to $\frac{\partial \vec{v}}{\partial t}$ regardless of the shape of the oscillating body. Therefore a disk with radius $R >> \delta$ can be considered infinite and the solution of the velocity distribution mirrors the one given above. Having said this, the torque on the oscillator due to the fluid is easily found by integrating in cylindrical coordinates for σ_{xy}:

$$L = 2L_1 = 2 \int_0^R r \sigma_{xy} 2\pi r \, dr \tag{4.11}$$

Where L_1 is the torque on either the upper or lower walls of the oscillator. The velocity is:

$$u_0 e^{-i\omega t} = r\dot{\Theta} \tag{4.12}$$

where the angular velocity is:

$$\dot{\Theta} = \Theta_0 e^{-i\omega t} \tag{4.13}$$

Now for the torque we get:

$$L = 2 \int_0^R \eta \frac{(1+i)}{\delta} \tan(kd/2) r\dot{\Theta} \, dr \tag{4.14}$$

so

$$L = \pi R^4 \dot{\Theta} k \eta \tan(kd/2) \tag{4.15}$$

Expanding for k we have:

$$L = \pi R^4 \dot{\Theta} \frac{(1+i)}{\delta} \eta \frac{\sin(d/\delta) + i\sinh(d/\delta)}{\cos(d/\delta) + i\sinh(d/\delta)} \tag{4.16}$$

or defining $x = d/\delta$ as Parpia does[25] we get:

$$L = \pi R^4 \dot{\Theta} \frac{\eta}{\delta} \left(\frac{\sin(x) - \sinh(x)}{\cos(x) + \cosh(x)} + i \frac{\sin(x) + \sinh(x)}{\cos(x) + \cosh(x)} \right) \tag{4.17}$$

Further we define:

$$f_1(x) = \frac{\sin(x) - \sinh(x)}{\cos(x) + \cosh(x)} \tag{4.18}$$

$$f_2(x) = \frac{\sin(x) + \sinh(x)}{\cos(x) + \cosh(x)} \tag{4.19}$$

We also have $\ddot{\Theta} = -i\omega\dot{\Theta}$ so the torque is:

$$L = -\beta_1 \dot{\Theta} - \beta_2 \ddot{\Theta} \tag{4.20}$$

where

$$\beta_1 = \pi R^4 \frac{\eta}{\delta} f_1(x) \tag{4.21}$$

$$\beta_2 = \frac{\pi R^4}{\omega} \frac{\eta}{\delta} f_2(x) \tag{4.22}$$

The moment of inertia of the fluid enclosed in the cavity of the oscillator is:

$$I_f = \frac{\pi}{2} \rho R^4 d \tag{4.23}$$

Therefore we have:

$$\beta_1 = I_f \omega \frac{f_1(x)}{x} \tag{4.24}$$

And:

$$\beta_2 = I_f \frac{f_2(x)}{x} \tag{4.25}$$

At this point we shall look at the equation of motion for the empty torsional oscillator:

$$I_0 \ddot{\Theta} + M\dot{\Theta} + N\Theta = D_0 e^{-i\omega t} \tag{4.26}$$

here I_0 is the moment of inertia of the empty oscillator, M is the damping, N is the torsional constant, and $D_0 e^{-i\omega t}$ is the driving force.

We see that the when the oscillator is filled up with fluid its equation of motion will be changed in such a way that β_1 will contribute to the damping, while β_2 increases the moment of inertia. The equation of motion for the full oscillator becomes:

$$(I_0 + \beta_2)\ddot{\Theta} + (M + \beta_1)\dot{\Theta} + N\Theta = D_0 e^{-i\omega t} \tag{4.27}$$

In the case when there is no driving torque ($D_0 e^{-i\omega t} = 0$), the solutions of the above equation are of the form:

$$\Theta = \Theta_0 e^{-t/\tau} e^{-i\omega t} \tag{4.28}$$

Substituting into the equation of motion we get complex equation for which the real part is:

$$(I_0 + \beta_2)\left(\frac{1}{\tau^2} - \omega^2\right) - \frac{(M + \beta_1)}{\tau} + N = 0 \tag{4.29}$$

and the imaginary part is:

$$\frac{2\omega(I_0+\beta_2)}{\tau} - (M+\beta_2)\omega = 0 \tag{4.30}$$

When the term with the moment of inertia is larger than the term with damping in the real part equation, we get:

$$\omega = \sqrt{\frac{N}{(I_0+\beta_2)}} \tag{4.31}$$

Similarly when the moment of inertia of the empty oscillator is much larger than that of the fluid, from the imaginary part equation we get:

$$\tau = \frac{2I_0}{M+\beta_1} \tag{4.32}$$

Now we are positioned to determine the quality factor Q of the oscillator. It is defined as:

$$Q = \frac{\omega\tau}{2} \tag{4.33}$$

Substituting for ω and τ we get:

$$Q^{-1} = \frac{\beta_1 + M}{\omega I_0} \tag{4.34}$$

We see that the dissipation of the fluid is added on top of the one from the empty oscillator. In order to find the quality factor only due to the fluid we define:

$$Q_f^{-1} = \frac{\beta_1}{\omega I_0} = Q^{-1} - \frac{M}{\omega I_0} \tag{4.35}$$

Thus now we have:

$$Q_f^{-1} = \frac{I_f}{I_0}\frac{f_1(x)}{x} \tag{4.36}$$

This can further be written in terms of the period shift of the full oscillator with respect to the empty one:

$$Q_f^{-1} = \frac{2\Delta P_0}{P_0}\frac{f_1(x)}{x} \tag{4.37}$$

where P_0 is the period of the empty oscillator and ΔP_0 is the shift of the period due to the additional fluid. For small values of x we have the approximation:

$$Q_f^{-1} = \frac{2\Delta P_0}{P_0}\frac{x^2}{6} \tag{4.38}$$

Or in terms of the film thickness and fluid parameters:

$$Q_f^{-1} = \frac{\Delta P_0}{P_0}\frac{d^2\rho\omega}{6\eta} \tag{4.39}$$

The solution for the equation of motion for the oscillator can also be represented as:

$$\Theta = A\cos(\omega_d t - \phi) \tag{4.40}$$

The phase is:

$$\phi = \arctan\left(\frac{Y}{X}\right) \tag{4.41}$$

and the amplitude is:

$$A = \sqrt{X^2 + Y^2} \tag{4.42}$$

Where:

$$X = \frac{D}{I}\frac{\frac{\omega_0\omega_D}{Q}}{(\omega_D^2 - \omega_0^2)^2 + \frac{\omega_0^2\omega_D^2}{Q^2}} \tag{4.43}$$

and

$$Y = -\frac{D}{I}\frac{\omega_D^2 - \omega_0^2}{(\omega_D^2 - \omega_0^2)^2 + \frac{\omega_0^2\omega_D^2}{Q^2}} \tag{4.44}$$

With these equations we are able to calculate the quality factor and the resonant frequency as they shift while the resonator is driven at a constant frequency ω_D. For the inferred quality factor we have:

$$Q_T = \left(\frac{X_T^2 + Y_T^2}{X_T}\right)\frac{Q_R}{A_R} \tag{4.45}$$

And the inferred resonant frequency is:

$$\omega_T = \omega_D\left(1 + \frac{Y_T}{2X_T Q_T}\right) \tag{4.46}$$

Where the amplitude A_R is determined when the oscillator is driven on resonance.

4.2 Slip

The most simplistic description of the velocity of a fluid past a boundary is that it decays exponentially from its bulk value to zero at the surface with a length scale as given by the viscous penetration depth in equation 4.9. However when the particles composing the fluid are dilute (or alternately in a Fermi liquid the excitations being dilute gas) there will be discrepancy from this description.

To distinguish between the different regimes the Knudsen number is defined as $K_N = \lambda/d$, where λ is the mean free path between particle collisions and d is the thickness of the film. If $\sim 0.01 > K_N$ the collisions are mainly between quasiparticles and other quasiparticles and the hydrodynamic regime can be used. In the ballistic regime when $K_N > 1$ the particles are much more likely to collide with the walls of the sample than with each other. For the intermediate

case of the Knudsen flow, $\sim 0.01 < \lambda/d < 1$ the collisions of the particles are affected both from the walls and other particles.

For a fluid with fixed thickness d, the mean free path is the parameter that governs the flow regime. The mean free path can be determined directly from the viscosity of the fluid (equation 4.48). Various experiments[3, 23, 5, 6] have determined the T^{-2} dependence of the viscosity for the normal ^3He. In particular from Wheatley[27] (figure 4.1) we obtain the mean free path at zero pressure as $\lambda \approx 68/T^2$, where the mean free path is in μm and the temperature is in mK.

We determine that the fluid in our cell will begin to enter the Knudsen regime at $100\,mK$ and will be in the hydrodynamic regime at higher temperatures.

In the slip theory[2] the velocity is finite at the surface but extrapolates to zero at the slip length ζ behind the surface. From the theory the slip length is proportional to λ. The correction of the slip theory to the oscillator equation is such that the viscosity η is replaced by an effective viscosity:

$$\frac{1}{\eta_{eff}} = \frac{1}{\eta}\left(1 + \frac{6\zeta}{d}\right) \tag{4.47}$$

The viscosity of the normal ^3He fluid in the Landau-Fermi liquid regime is given by:

$$\eta = \frac{1}{5} n p_F \lambda \tag{4.48}$$

where n is the number density and p_F is the Fermi momentum. Thus we have:

$$\frac{1}{\eta_{eff}} = \frac{1}{\eta} + \frac{30}{n p_F d}\left(\frac{\zeta}{\lambda}\right) \tag{4.49}$$

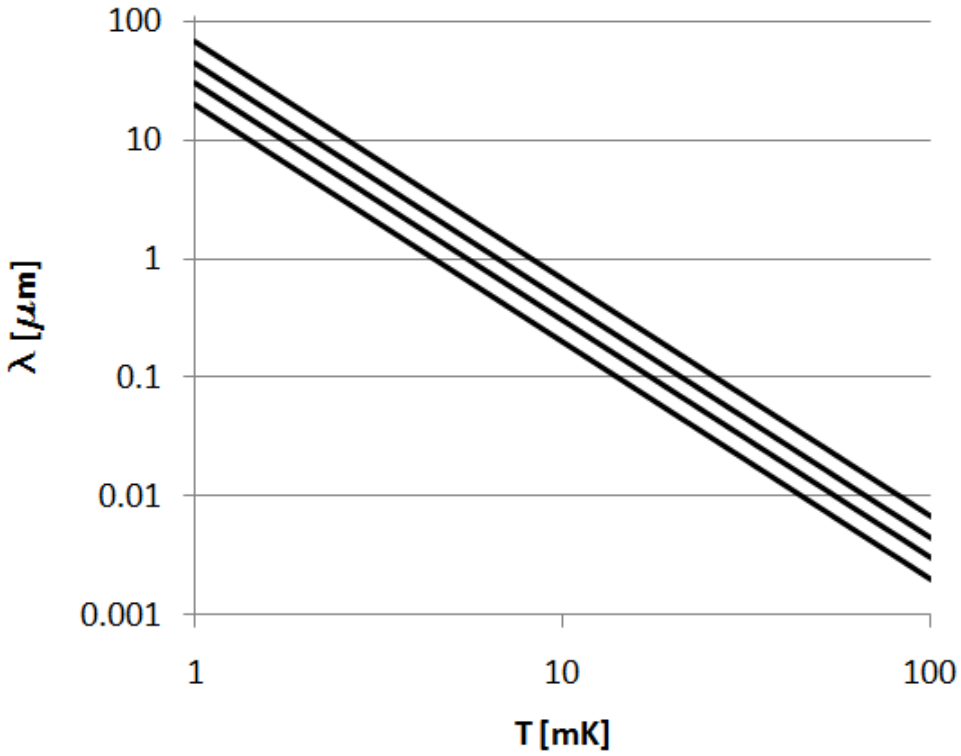

Figure 4.1: Quasiparticle mean free path as a function of temperature and pressure. From top to bottom the lines correspond to: 0bar, 9bar, 21bar and 34.4bar[27].

For a given surface we can consider that a fraction s of the quasiparticles of the ^3He are scattered specularly and the remaining fraction $1-s$ are scattered diffusely. From the slip theory for ^3He then we have:

$$\frac{\zeta}{\lambda} = 0.582\left(\frac{1+s}{1-s}\right) \tag{4.50}$$

Thus for the effective viscosity we get:

$$\frac{1}{\eta_{eff}} = \frac{1}{\eta} + \frac{17.46}{np_F d}\left(\frac{1+s}{1-s}\right) \tag{4.51}$$

From this equation we see that the viscosity of the fluid is strongly dependent on the types of scattering present.

4.3 Description of the experiment

The dimensions of the oscillator are given as shown in chapter 2. The dimensions have been chosen as a compromise between the available space on the cryostat for mounting the experiment, the degree of difficulty to machine the torsional rod and most importantly the requirement that the low frequency vibrational noise be reduced.

As the oscillator has two torsional rods it has two distinct torsional modes with distinct frequency. For the lower frequency the oscillator is in its symmetric mode where the head of the oscillator and the central part with the wings move in phase. For the antisymmetric mode the resonant frequency is higher and the two sections of the oscillator move out of phase.

To determine the corresponding resonant frequencies the torsional constant of a rod is given by:

$$k_{torsion} = \frac{\pi(D_{out}^4 - D_{in}^4)G}{32L} \tag{4.52}$$

where the inner diameter of the rod is D_{in}, the outer diameter is D_{out}, the length is L and the torsional modulus is G. For coin silver the torsional modulus is $G = 30\,GPa$.

With the parameters that we have, the resonator has been constructed to have the antisymmetric mode at about three times the frequency of the symmetric mode. The symmetric mode acts as a filter for the external vibrations introduced to the oscillator. After building the complete oscillator we have measured the antisymmetric mode to be at $\nu_s = 1287\,Hz$ and the symmetric mode at $\nu_a = 460\,Hz$.

Since the moment of inertia of the cell is $I_{cell} = 1.5\,g\,cm^2$ and the moment of inertia of the normal ^3He liquid inside the cavity is $I_{He} = 4.2 \cdot 10^{-7}\,g\,cm^2$, the maximum expected frequency shift between the loaded and empty oscillator will be when the fluid is completely locked and we will have:

$$\frac{\Delta\nu}{\nu} = -\frac{1}{2}\frac{\Delta I}{I} = -\frac{I_{He}}{2I_{cell}} = -1.4 \cdot 10^{-7} \tag{4.53}$$

4.4 Measurements

The oscillator is connected to a constant drive circuit as shown on figure 4.2. The filter is set to remove frequencies below $1000\,Hz$ and above $1580\,Hz$. The two channel SR830 lock-in amplifier compares the detected signal with the drive signal. Channel X measures the component of the signal that is $\pi/2$ out of phase with the drive signal, and channel Y measures the component that is in phase. These two channels are sufficient to determine the phase angle and the amplitude as given in equations 4.41 and 4.42. The measurements are recorded and the equipment is controlled through the GPIB interface of a computer.

Since the equation of the oscillator that we use is linear in Θ we measured its response with respect to different driving amplitudes and selected level for which the response is safely in the linear regime. The drive voltage that we selected is $10\,mV$ peak to peak.

After the empty oscillator is cooled to its operational temperatures the resonance peak is characterized by slowly sweeping the frequency around it. The amplitude, quality factor and resonance frequency are noted and entered into equations 4.45 and 4.46. The function generator is set at the measured resonant

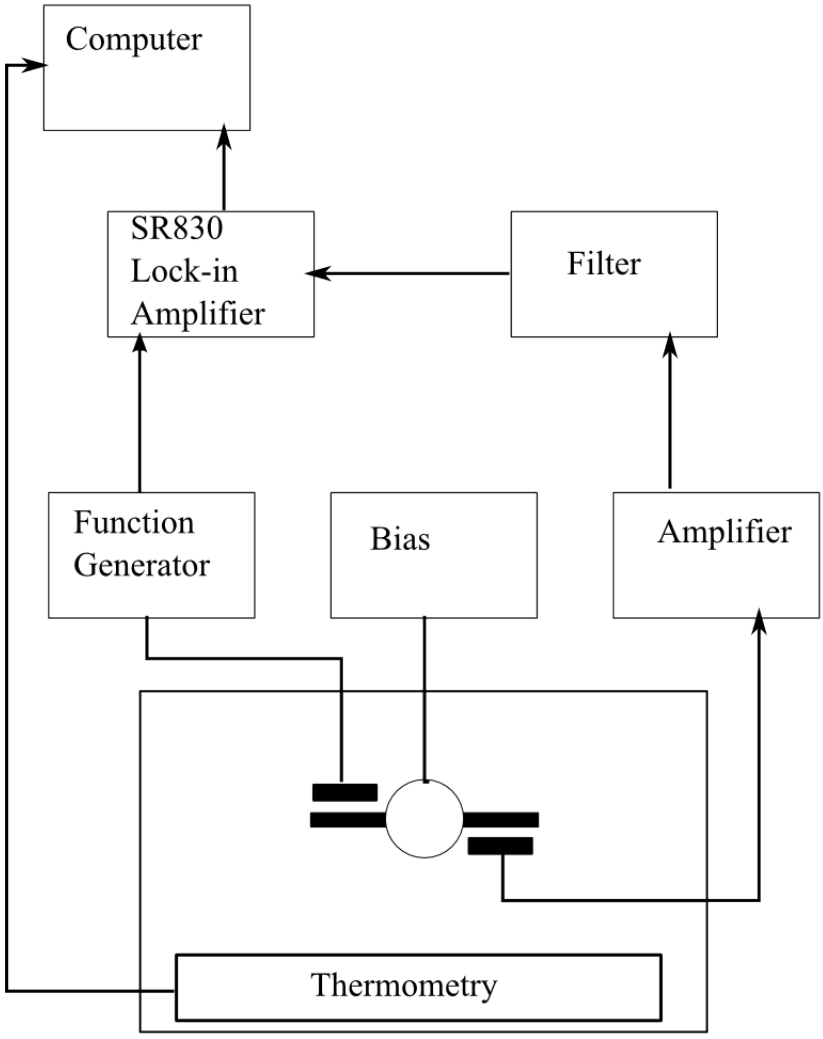

Figure 4.2: Diagram of the electronics used to run the experiment.

frequency and the electronics is engaged to continuously measure the temperature of the experiment and the X and Y channels of the lock-in amplifier. The temperature then is slowly varied and the resonance frequency and quality factor of the torsional oscillator are inferred as described above.

After the background of the oscillator with the empty cell is determined ^3He is admitted through the gas handling system. We infer when the experiment is fully loaded by observing the drop of the pressure in the buffer tanks containing the portion of all of the helium gas. When the pressure is stable for several hours we consider the cell to be fully loaded.

When the required amount of helium is condensed we repeat the measurements for the frequency response and the quality factor for the loaded oscillator at several different pressures of the ^3He.

4.5 Results and discussion

The measurements of the full and empty cell are given on the same plots. The data for the frequency shift is given in figure 4.3 and the quality factor is given in fugure 4.4.

After taking the data we have subtracted the measured frequency shift from the expected frequency shift of the fully loaded cell (figure 4.5). As observed from the graph we see no change in the frequency shift below $100\,mK$ of the filled oscillator compared to the empty oscillator. The measured frequency shift at $160\,mK$ corresponds to mass loading of roughly 55% of the available fluid.

After subtracting the background of the empty oscillator the dissipation of

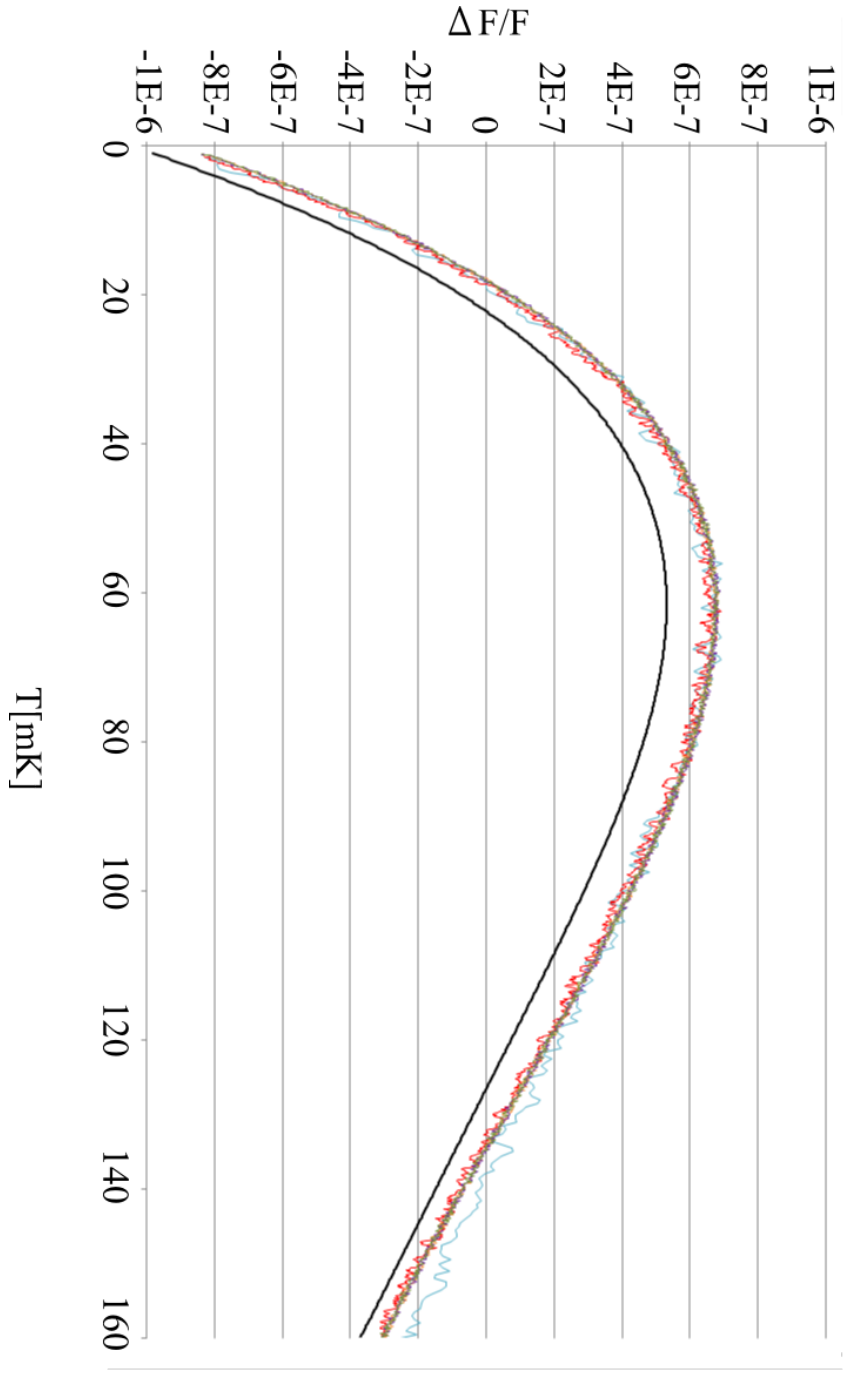

Figure 4.3: Fractional frequency shift of the oscillator. Blue line is data for the empty oscillator, black line is the expected response for fully locked helium, the rest is data of resonator when pressurized (up to 30 psi).

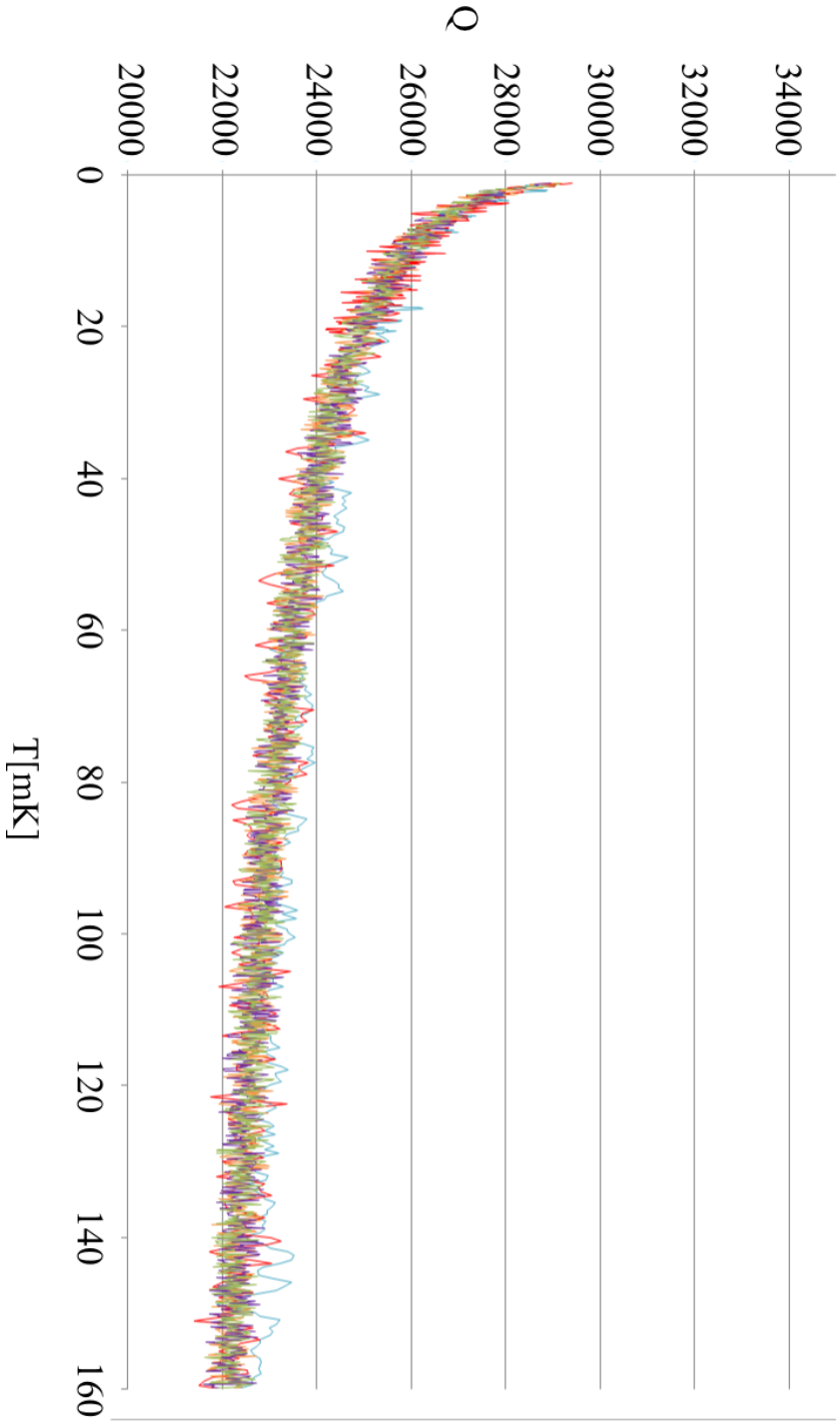

Figure 4.4: The quality factor of the oscillator. Blue line is data for the empty oscillator the rest is data of resonator when pressurized (up to 30 psi).

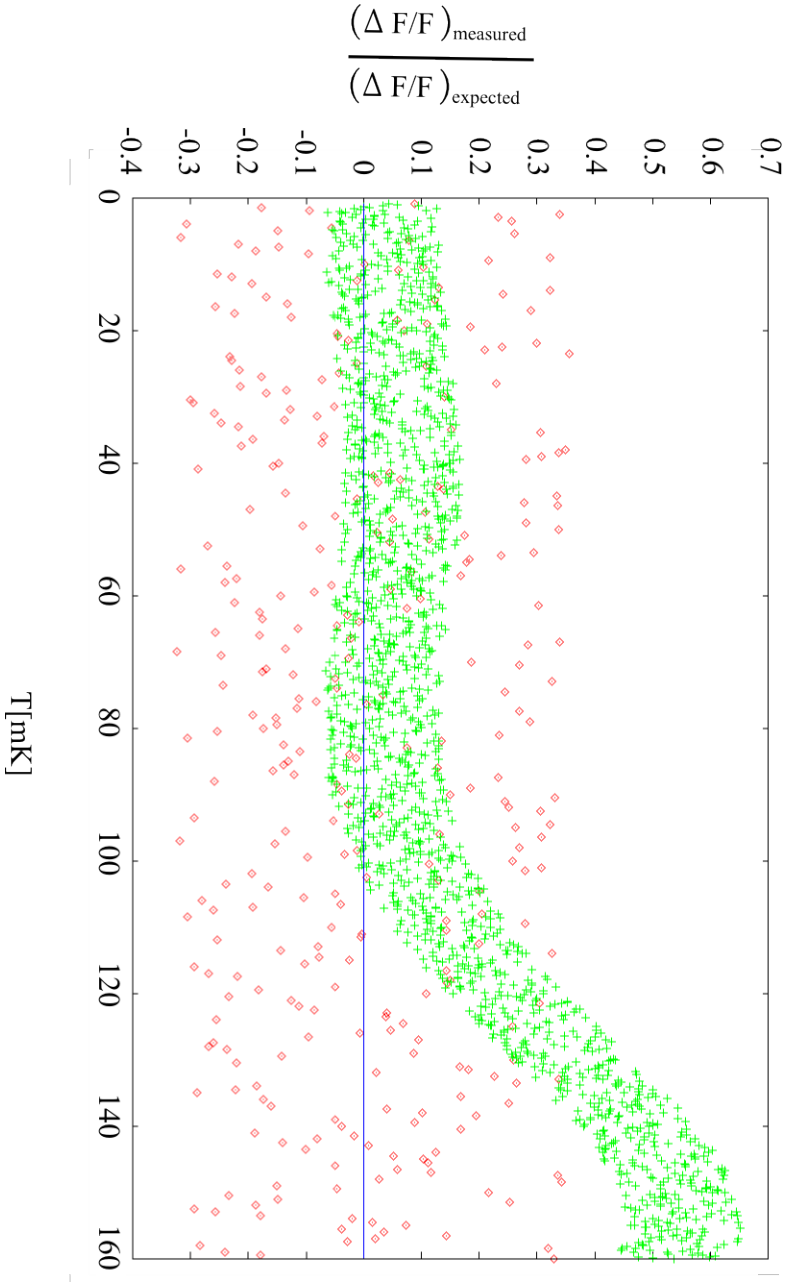

Figure 4.5: Fraction of the fluid mass coupled to the oscillator. The red points are from the empty cell and the green points are for the cell loaded with ^3He at 0bar.

the loaded oscillator is given in figure 4.6. While the dissipation for the loaded cell seems to increase when the temperature is higher we can not attribute this increase to the dissipation of the liquid ^3He. The maximum expected dissipation of the helium is determined by maximizing equation 4.55 ($\omega\tau = 1$) and is $\Delta(1/Q) = 1.4 \cdot 10^{-7}$, substantially less than the observed deviation. Moreover the dissipation data of the loaded cell is completely in the error bounds of the empty oscillator data.

Given that the viscous penetration depth $\delta \sim 7400\,nm$ at $100\,mK$ is much larger than the thickness of the film constrained in the cell, in the absence of slip we expected the fluid to move as a rigid object with the cell and give full mass loading for a considerable range of the temperatures investigated. Our measurements thus come as quite an unexpected finding.

Since the surfaces of the cell are highly polished the level of specular scattering for the particles of the liquid will be considerable. As the momentum of the particles does not change during specular scattering, no momentum will be transferred to the liquid from the walls of the cavity and the fluid will decouple and will remain stationary in the laboratory frame.

We relate our experiment to one done by Casey. In that experiment torsional oscillator with a head made out of highly polished coin silver flats is loaded with ^3He films with variable thickness between $40\,nm$ and $290\,nm$. The oscillator is driven at $2841\,Hz$. The films are grown on each of the silver surfaces and each of them has one free surface. The results of their measurements for the frequency shift and the dissipation due to the helium films are given in figure 4.7.

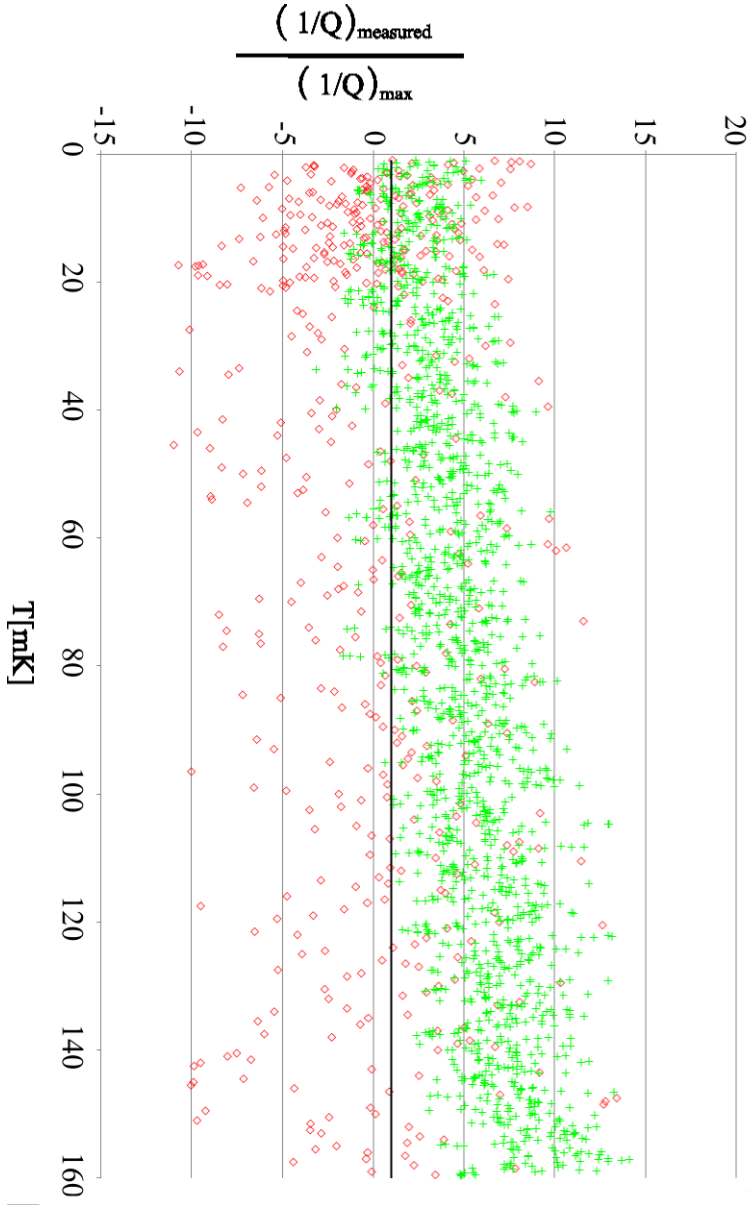

Figure 4.6: Fractional dissipation of the oscillator as compared to the maximum expected dissipation. The red points are from the empty cell and the green points are for the cell loaded with ^3He at zero pressure. The black line corresponds to the expected maximum dissipation.

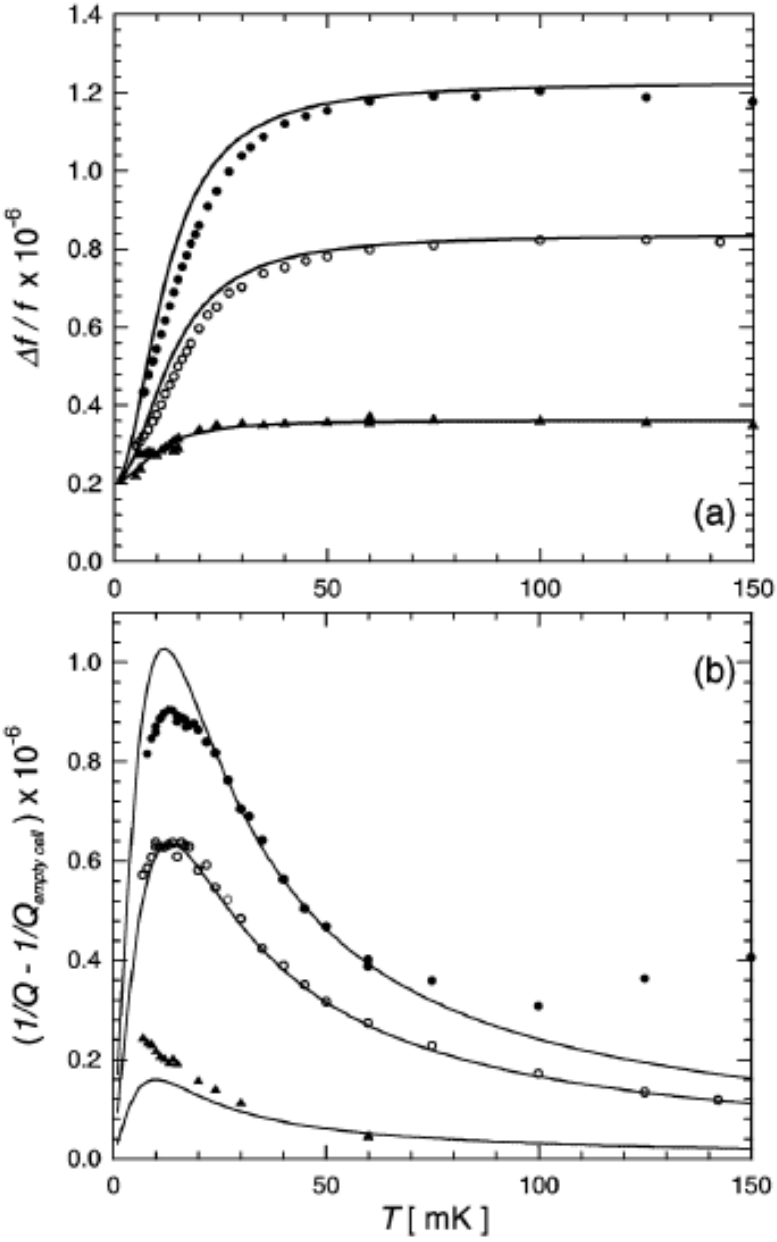

Figure 4.7: (a) Fractional frequency shift and (b) dissipation due to ^3He films with different thickness as measured by Casey et all (after Casey et. al. [10]).

It is seen that at high temperatures the helium is coupled rigidly with the oscillator. However as the temperature is lowered the frequency shift decreases indicating that the film begins to decouple from the oscillator accompanied with increase in the dissipation. This is modelled by describing the helium as a rigid slab coupled to the oscillator by interfacial friction. From the equations of motion for slab with mass m and substrate with mass M the frequency shift and dissipation change can be determined:

$$\frac{\Delta f}{f_0} = -\frac{m}{2M\left(1 + (\omega\tau)^2\right)} \tag{4.54}$$

$$\Delta\frac{1}{Q} = \frac{m\omega\tau}{M\left(1 + (\omega\tau)^2\right)} \tag{4.55}$$

where the momentum relaxation time τ between the ^3He slab and the oscillator is temperature dependent. Plotting $\omega\tau$ as a function of the inverse temperature (figure 4.8) reveals that the decoupling is due to the increase of τ as the temperature is decreased. Below $100\,mK$ the relaxation time is nearly inversely proportional to the temperature and is very weakly dependent on the film thickness.

The dependence of the relaxation time on the inverse temperature can be understood by considering the effects of the surface scattering. Theoretical work by Meyerovich and Stepaniants[24] shows that the boundary induced transition probability is determined by the surface characteristics of the boundary. More specifically it shown that a surface with gaussian correlations over length R and roughness amplitude l gives:

$$\frac{1}{\tau} = 3\left(\frac{1}{\tau_\eta\tau_F}\right)^{1/2}\left(\frac{l}{R}\right)^2\frac{1}{k_F d} \tag{4.56}$$

where d is the film thickness and τ_η is the quasiparticle relaxation time, $\tau_F = \frac{\hbar}{2E_F}$ with k_F the Fermi wave vector and E_F the Fermi energy.

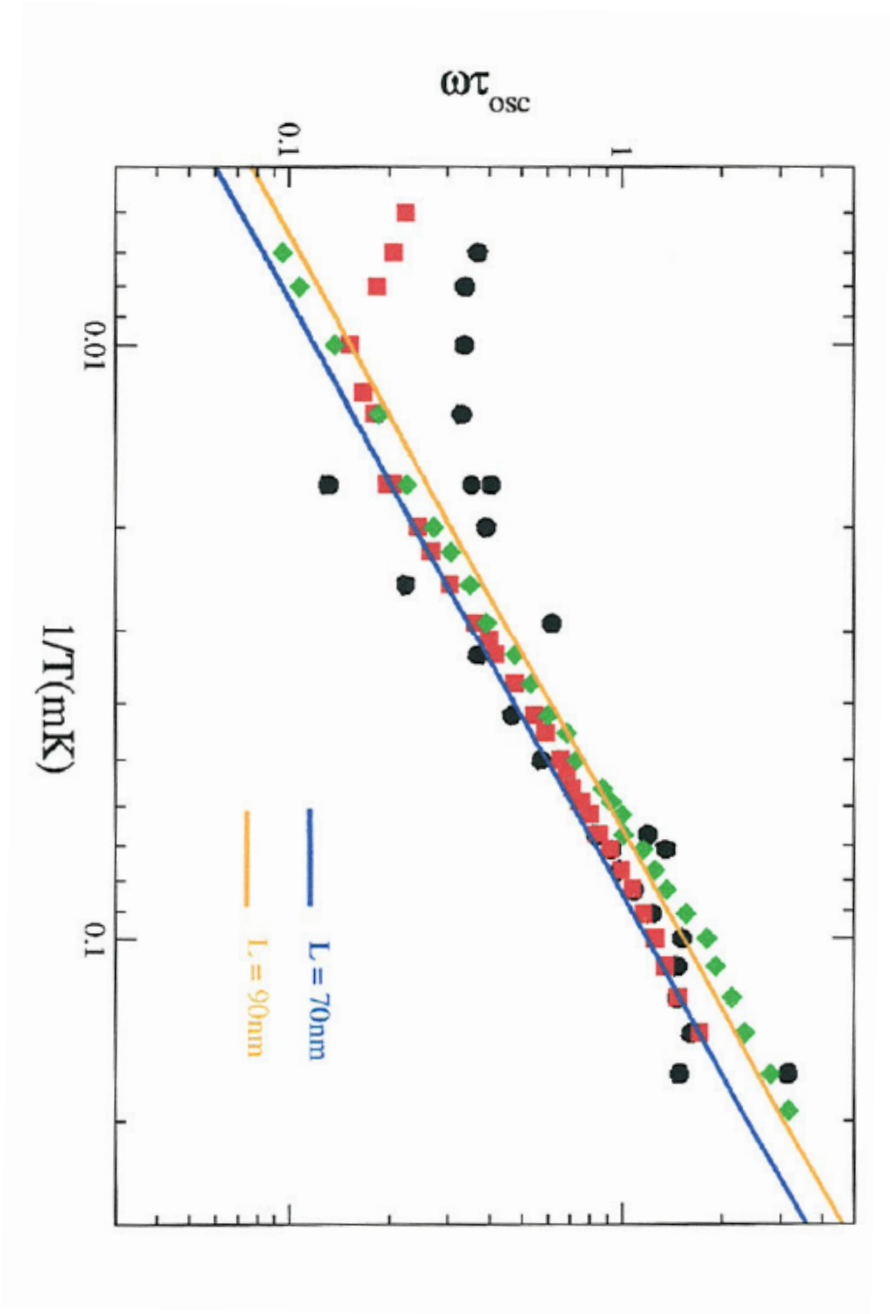

Figure 4.8: (Comparison of $\omega\tau_{osc}$ as measured by Casey et all. for films with thickness between 40 – 290nm and theoretical prediction by Meyerovich and Stepaniants.

Since τ_η is inversely proportional to T^2 the derivation accounts for the temperature dependence of the moment relaxation time. However the theory does not explain properly the independence of the relaxation time on the film thickness.

Nevertheless having τ that is parameterized by the surface characteristics we can juxtapose the results obtained in our experiment to those obtained by Casey et all.

We have managed to obtain a sample of the polished coin silver that Casey used in their experiment and compared it to the surfaces of the cell of our experiment. The comparison as described in chapter 3 shows that the topography of the surfaces for our experiment is sufficiently different from the polished silver.

The analysis of the surfaces show that:

$$\begin{aligned} \left(\frac{R}{l}\right)_{Borofloat} &= 2.79 \\ \left(\frac{R}{l}\right)_{Silver} &= 9.27 \end{aligned} \tag{4.57}$$

Given these results and considering the Meyerovich and Stepaniants theory we would expect the relaxation time for our experiment to be about 11 times shorter than the relaxation time in Casey. Since the frequency of our oscillator is only 2.2 times smaller than the frequency of the silver oscillator, the product $\omega\tau$ for our case will be 5 times smaller than for Casey and the ^3He film is expected to decouple less from the oscillator in our case.

In the light of this the Meyerovich and Stepaniants theory may not be fully applicable to our case. Even though it has properly predicted the inverse dependence of the relaxation time and the temperature it has not fitted properly the behavior of τ with the thickness of the film as measured experimentally.

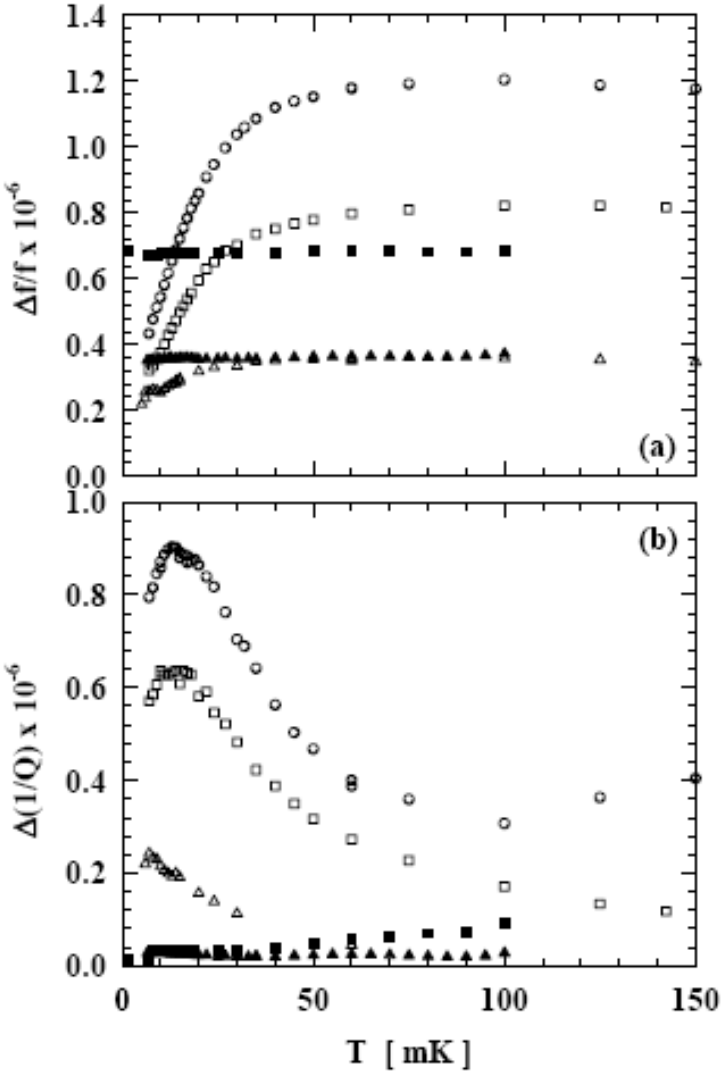

Figure 4.9: (a) Fractional frequency shift and (b) dissipation due to ^3He films with different thickness as measured by Casey et all. The dark symbols are for data of an oscillator with additional roughness on the surfaces (after Casey et. al.[11]).

4.6 Future Work

As the ultimate goal to produce the current oscillator was to study the transitions between the A and B phases of the two-dimensional superfluid ^3He we need to distinguish the signal of the fluid coupled to the oscillator from the background of the empty oscillator the current experiment needs refinement.

The decoupling of the fluid may be solved by changing the roughness parameters of the glass and silicon of the cell. We have shown that the roughness of the borosilicate glass can be increased by immersing it in dilute buffered oxide etch. To change the roughness of the silicon, photolithography can be employed to create pattern with the required characteristics. Another approach to keep the helium locked is to introduce fluid containing latex micro-beads in the already built cell and then evaporate the fluid to have only the beads in the cavity.

Encouraging results have been obtained in a separate experiment by Casey et all. for the detection of the superfluid ^3He by changing the surface properties of the plates. In that experiment silver particles with nominal size $700nm$ have been bonded on the surface of the silver plates. Measurements of the behavior of that oscillator revealed that the normal fluid has been coupled well to the oscillator (figure 4.9).

Unfortunately the fragile nature of the oscillator that we built did not survive the warming up procedures and the silicon was cracked near the joint with the torsional rod. Future work will require the cell for the head to be rebuilt, preferably with new surface characteristics created during the micro fabrication phase.

BIBLIOGRAPHY

[1] D. S. Greywall, Phys. Rev. B **33**, 7520 (1986)

[2] D.Einzel et al., J. Low Temp. Phys. **53**, 695 (1983).

[3] J.P.Eisenstein, G.W. Swift and R.E. Packard, Phys. Rev. Lett. **45**, 1199 (1980).

[4] H.E.Hall, in *Proc. of the European Phys. Soc., Haifa, 1974*, edited by C.G Kuper, S.G. Lipson and M. Revzen (Wiley and Sons, New York, 1974).

[5] D.A.Ritchie, J.Saunders, and D.F.Brewer, Phys. Rev. Lett. **59**, 465 (1987).

[6] D.C.Carless et al., J. Low Temp. Phys. **50**, 583 (1983).

[7] D.S.Betts, D.F.Brewer and R. Lucking, in *Proc. of 13th Intl. Conf of Low Temp. Phys., Boulder, Colorado, 1972*, edited by K.D.Timmerhaus, W.J. O'Sullivan and E.F. Hammel (Plenum, New York, 1976).

[8] M.R.Freeman et al., Phys. Rev. Lett. **60**, 596 (1988) and M.R.Freeman and R.C.Richardson Phys.Rev. B **41**, 1101 (1990).

[9] S.M.Tholen, Ph.D. Thesis, Cornell University (1992).

[10] A.Casey et al., Phys. Rev. Lett. **92**, 255301 (2004).

[11] A.Casey et al., in *Proc. of 24th Intl. Conf of Low Temp. Phys.*, edited by Y.Takano, S.P.Hershfield, S.O.Hill, P.J.Hirschfeld, and A.M.Goldman.

[12] J. Bardeen, L. N. Cooper, and J. R. Schreffer, Physical Review, **108**, 1175 (1957)

[13] Wen-Pin Shih, Chung-Yuen Hui and Norman C. Tien, J. Appl. Phys. **95**, 2800 (2004).

[14] D. I. Pomerantz, US Patent No. 3,397,287 (1968), US Patent No. 3,417,459 (1968).

[15] L. D. Landau and E. M. Lifshitz, *Fluid Mechanics* (Pergamon Press, 1959).

[16] Donald L. Smith and Andrew S. Alimonda, J. Electrochem. Soc. **140**, 1496 (1993).

[17] Ying-Hong Li and Tin-Lun Ho, Phys. Rev. B **38**, 2362 (1988).

[18] J. E. Berthold, R. W. Giannetta, E. N. Smith, and J. D. Reppy, Phys. Rev. Lett. **37**, 1138 (1976).

[19] A. B. Vorontsov and J. A. Sauls, Phys. Rev. B **68**, 064508 (2003).

[20] Y. Nagato and K. Nagai, Physica B **284**, 269 (2000).

[21] B. E. Deal and A. S. Grove, J. Appl. Phys. **36**, 3770 (1965).

[22] R. G. Bennet, Ph.D. Thesis, Royal Holloway University of London (2009) and to be published.

[23] J. M. Parpia and T. L. Rhodes, Phys. Rev. Lett. **51** 805 (1983).

[24] A. E. Meyerovich and A. Stepaniants, J. Phys.: Condens. Matter. **12**, 5575 (2000).

[25] J. M. Parpia, Ph.D. Thesis, Cornell University (1979).

[26] B. E. Deal and M. Sklar, J. Electrochem. Soc. **112**, 367 (1965).

[27] J. C. Wheatley, Rev. Mod. Phys. **47**, 415 (1975).